

1 **Geological evidence confirms the staircase patterns of Earth's**
2 **rotation deceleration from the Neoproterozoic to the Mesozoic Era**

3 He Huang^{1,2,3}, Chao Ma^{1,2,*}, Jacques Laskar³, Matthias Sinnesael³, Mohammad
4 Farhat³, Nam H. Hoang³, Yuan Gao⁴, Christian Zeeden⁵, Hanting Zhong^{1,2}, Mingcai
5 Hou^{1,2}, Chengshan Wang⁴

6 ¹ State Key Laboratory of Oil and Gas Reservoir Geology and Exploitation, Institute of
7 Sedimentary Geology, Chengdu University of Technology, Chengdu 610059, China

8 ² Key Laboratory of Deep-time Geography and Environment Reconstruction and Applications
9 of Ministry of Natural Resources, Chengdu University of Technology, Chengdu 610059,
10 China

11 ³ IMCCE, CNRS, Observatoire de Paris, PSL University, Sorbonne Université, 75014, Paris,
12 France

13 ⁴ State Key Laboratory of Biogeology and Environmental Geology, China University of
14 Geosciences (Beijing), Beijing 100083, China

15 ⁵ LIAG-Leibniz Institute for Applied Geophysics, Stilleweg 2, 30655 Hannover, Germany

16

17 **Author Contributions:** H.H., C.M., and J.L. formulated the original hypothesis and designed
18 the project. H.H. and C.M. performed all the Monte Carlo analyses. H.H. collected the data.
19 H.H., C.M., J.L., M.S., M.F. N. H., and Y.G. contributed to the data processing and
20 interpretation. All authors contributed to the data interpretation and to the preparation of the
21 manuscript.

22 Corresponding author: Chao Ma

23 Email: machao@cdut.edu.cn

24 **The paper is a non-peer reviewed preprint submitted to EarthArXiv.**

25

26

27 **Abstract**

28 Due to tidal dissipation, the Earth's rotation has been slowing down, but the past rates
29 of this process remain subject of debate. Here we conducted a comprehensive
30 cyclostratigraphic analysis of eight geological datasets to further constrain the Earth's
31 rotation history from the Neoproterozoic to Mesozoic. Our results allow us to further
32 test theoretical physical tidal models, and support a suggested stair-shaped Earth's
33 rotation deceleration pattern during 650-280 Ma, thereby increasing the Earth-Moon
34 distance about 20,000 km and the length of solar day approximately 2.2 hours.
35 Specifically, the high rate of Earth's rotation deceleration from 650 Ma to 500 Ma can
36 be attributed to the enhanced tidal resonance. In contrast, the unusually low tidal
37 dissipation during 500-350 Ma has led to a flatter trend of Earth's rotation
38 deceleration, closely followed by another high rate of Earth's rotation deceleration
39 during 350-280 Ma. These changes in Earth's rotation are closely linked to alterations
40 in Earth's tectonic contexts and ocean tidal resonance. Hence, we speculate that there
41 might be a relationship between the Earth's rotation and geological processes.

42 **Keywords:** Earth-Moon system, Earth's rotation, cyclostratigraphy, tidal resonances,
43 geological processes

44 **Introduction**

45 Due to the tidal interplay in the Earth-Moon system, and by virtue of angular
46 momentum conservation, the Earth's rotational angular momentum is transferred to
47 the orbital counterpart of the Moon (1). Consequently, the deceleration of Earth's
48 rotation and the gradual orbital recession of the Moon constitute an ongoing process
49 that has persisted since the formation of the Earth-Moon system to the present day.
50 However, the deceleration rate of Earth's rotation has changed over time and appears
51 to have exhibited a nonlinear pattern, as suggested by geological observations (2-5).
52 The Earth's rotational motion can be described by its axial precession frequency,
53 which gives the change in orientation of the spin in arc seconds per year (arcsec/yr,
54 denoted as p following ref. (6)). The present value of p is measured with high
55 precision (50.475838 arcsec/yr) (6), but the evolution history of the Earth's rotational

56 motion is largely unknown. Apollo's Lunar laser ranging (LLR) observations of
57 today's Lunar recession rate (~ 3.83 cm/yr) (7) and the age of the Moon (~ 4.425 billion
58 years ago (Ga)) (8) provide two constraints on Lunar recession history. However,
59 combining the models of bodily tides with the present LLR measurements, one would
60 predict a collision between the Moon and Earth at ~ 1.5 Ga (9, 10), which is obviously
61 incompatible with the lunar age inferred from radioisotopic dating analyses (8, 11,
62 12). Several studies have proposed various solutions to solve this paradox by using
63 analytical models, numerical simulations and observational geological data (10, 13-
64 16). However, as the current theoretical tidal models are short of being comprehensive
65 in describing dissipative processes, reliable observational geological data are crucial
66 for further constraining theoretical model predictions.

67 Over the past few decades, a series of empirical geological records have been reported
68 to reconstruct the Earth's astronomical properties, such as the number of days per
69 lunar month inferred from tidalites (5, 17, 18), and the number of days per solar year
70 calculated from growth rings of invertebrate fossils (2, 19-22). Although the analysis
71 of tidalites and invertebrate fossils is undoubtedly meaningful and improves our
72 understanding of the Earth's rotation history (23), both of them exhibit large
73 uncertainties in cycle interpretation and counting (5, 23-25), which might result in
74 inconsistencies with the true situation of Earth's rotational properties and even give
75 incorrect reconstruction of the Earth-Moon evolution (review in ref. 24). For instance,
76 the Lunar semimajor axis deduced from Weeli-wolli tidal rhythmmites at 2450 Ma ago
77 were interpreted differently by Walker and Zahnle (26), and Williams (5). Walker and
78 Zahnle identified them as indicative of Lunar nodal precession, whereas Williams
79 interpreted the periodic sedimentary features as representative of spring-neap tides
80 occurring within an annual cycle. Similar incompatible interpretations of the same
81 record can also be noticed in the case of the Cottonwood tidal rhythmmites at 900 Ma
82 (17, 27) and the Elatina tidal rhythmmites at 620 Ma (5, 17, 28).

83 With recent developments in cyclostratigraphy, we can extract the Earth's
84 astronomical properties from astronomically-forced stratigraphic records using more

85 robust quantitative methods (29-31). Consequently, over the past years, numerous p
86 values accompanied by uncertainty estimations have been reported (29-35). These
87 contributions have substantially enriched our understanding of the history of Earth-
88 Moon evolution. To date, it seems that astronomically-forced cyclostratigraphic
89 records might be the most robust archives for deciphering past changes in Earth's
90 rotation and Lunar recession history (24), especially if amplitude relationships
91 between precession and eccentricity can be demonstrated. However, it remains
92 essential to continue gathering reliable geological data to independently test physical
93 tidal models. This is particularly crucial in the critical periods that align with modeled
94 prediction of significant astronomical variations that are driven by oceanic tidal
95 resonances (16) or the atmospheric thermal tidal locking hypothesis during the boring
96 billion period (1.8-0.8 Ga) (24, 36). Here, we use the Monte Carlo Markov Chain
97 (MCMC) Bayesian inversion method developed by ref. (29) (i.e., TimeOptMCMC,
98 see Methods) to compute the p -values from eight high-fidelity cyclostratigraphic time
99 series covering ages ranging from 245 Ma to 570 Ma (32, 37-43) (*SI Appendix*, Table
100 S1, Fig. S1-S8). These new p -values, along with other published p -values, have nicely
101 constrained the Earth's rotation history from the Neoproterozoic to the Mesozoic Era
102 and served as an independent way to test the theoretical physical tidal models.

103 **Results**

104 **Cyclostratigraphic datasets compilation**

105 Through multiple cyclostratigraphic analyses and tests (see Methods), we identified
106 eight high-fidelity datasets from the literature (excluding those analyzed by refs. (29,
107 34)) that were suitable for TimeOptMCMC analysis (the detailed analysis parameters
108 refer to *SI Appendix*, Table S1 and Supplementary R scripts). The detailed
109 information of these datasets is as follows: (I) The Guandao section was deposited
110 in a marine environment during the latest Permian through the earliest Late Triassic
111 (36). A ~260 m gamma ray (GR) data was retrieved from this section for
112 cyclostratigraphic analysis (37). Variations in GR relate to the terrestrial input and
113 marine productivity, which controlled by the astronomical forcing (37). We chose the

114 10-72 m interval (~245 Ma) to run the TimeOptMCMC simulation. (II) The Permian
115 Lucaogou Formation (~290 Ma) developed in a lacustrine environment, and mainly
116 consisting of shale facies with thin beds of dolomitic siltstone as a minor lithology.
117 The log natural gamma ray (GR) data show strong variations associated with the
118 orbital forcing (32). We chose the 3650-3770 m interval to perform the
119 TimeOptMCMC analyses. (III) The H-32 drilling core in Iowa recorded a positive
120 $\delta^{13}\text{C}$ excursion associated with the Frasnian–Famennian (F–F) boundary during the
121 Upper Devonian (38). The magnetic susceptibility (MS) data revealed quasi-periodic
122 signals at eccentricity, obliquity and precession bands (38). Although the precession
123 band signals are not obvious (Fig. S3), we still chose the 1.76-9 m interval (~375 Ma)
124 for TimeOptMCMC analyses. This choice was necessitated by the absence of any
125 other available cyclostratigraphic dataset capable of reconstructing Earth’s rotation
126 rate within the time frame spanning from 290 Ma to 410 Ma (Figs. 1, 2).
127 Consequently, it plays a crucial role in constraining potential trends in Earth’s rotation
128 deceleration trajectory during this period, although the reconstructed *p*-value features
129 a relatively high uncertainty (Table 1). (IV) The Požár-CS limestone section has a
130 thickness of 118 m, covering the Lochkov and Praha Formations. High resolution MS
131 was measured from this section by Da Silva et al. (39). Cyclostratigraphic analyses of
132 the MS data revealed obvious Milankovitch signals (39). We chose the 106.7-114 m
133 interval (~410 Ma) for TimeOptMCMC analyses. (V) In Anticosti Island, Canada, a
134 remarkably well-preserved and substantial Upper Ordovician reference section was
135 deposited within a structural embayment situated along the eastern margin of
136 Laurentia. The Vauréal Formation, belonging to the upper Katian Stage primarily
137 comprises interbedded micrite, calcarenite, and marl, exhibiting astronomically-forced
138 lithological associations (40). High-resolution potassium (K%) was measured for
139 reflecting the multimeter cycles of carbonate versus clay lithology (40). Here, we
140 chose the 550-900 m interval (~448 Ma) for the TimeOptMCMC analysis. (VI) The
141 Liangjiashan section, located along the margin of the North China Block, represents
142 the deposition of shallow marine carbonate during the Early Ordovician period. A set
143 of 1024 geochemical data points derived from X-ray fluorescence (XRF) analysis was

144 obtained at the Liangjiashan section (41). These data encompassed the elemental
145 composition of Ti, Si, Fe, and Ca. Milankovitch cycles have been identified in the
146 Liangjiashan section by analyzing the Ca% (41). Here, we chose the 45-62 m interval
147 (~470 Ma) for the TimeOptMCMC analyses. (VII) The Alum Shale Formation is
148 primarily composed of laminated, organic-rich mudstone characterized by a
149 substantial presence of pyrite. The elemental abundances retrieved from high
150 resolution core scanning XRF analysis (42). By analyzing the S% composition, a
151 floating timescale calibrated to the stable 405 kyr eccentricity cycle was established
152 for an approximately 8.7 Ma interval spanning the Miaolingian-Furongian boundary
153 (42). Here, we chose the 83-85.5 m (~493Ma) interval for TimeOptMCMC analyses.
154 (VIII) The Doushantuo Formation was deposited on the inner shelf of the Ediacaran
155 Yangtze Platform at the Zhengjiatang section. Within this section, high-resolution MS
156 series were obtained from the stratigraphic interval containing the Shuram carbon
157 isotope excursion (CIE) (43). Power spectral analyses conducted on the MS series of
158 the carbonate rocks demonstrate periodicities that align closely with the Milankovitch
159 cycles at ~570 Ma (43). Here, we chose the 26-33 m interval to perform the
160 TimeOptMCMC analyses.

161 **The TimeOptMCMC analysis results**

162 By running the TimeOptMCMC analysis, the prior distributions of the sedimentation
163 rate (SR) inherited from the original literature and also further independently
164 constrained by the TimeOpt analysis, while the p ranges were obtained from the tidal
165 model of Waltham (13) (see Methods, *SI Appendix*, Table S2). The TimeOptMCMC
166 results of eight cyclostratigraphic time series are shown here (Table 1, Fig. 1). The
167 blue histograms depict the posterior distributions of the SR and p , while prior
168 distributions are in grey (Fig. 1). Comparing the two distributions, it becomes evident
169 that the posterior distributions are more confined compared to the prior distributions
170 (Fig. 1). This outcome signifies the successful optimization of SR, p , and the
171 fundamental secular frequencies g_i terms by the TimeOptMCMC. The mean value
172 and standard deviation (σ) of SR and p were calculated from the after burn-in results

173 from the MCMC simulation results (Table 1). According to the p value, we can derive
174 the Earth-Moon distance (EMD), the length of the solar day (LOD) and Earth's
175 obliquity angle according to the model of Farhat et al. (16) using the tool provided on
176 the *AstroGeo* website (<http://www.astrogeo.eu/>) (Table 1, *SI Appendix*, Fig. S10). For
177 example, the TimeOptMCMC analysis generates a posterior distribution that
178 determines Earth precession rate at 56.70 ± 2.26 arcsec/yr at 245 Ma (Table 1). This
179 observation is consistent with an EMD of 373.99 (+3.36/-3.22) thousand kilometers, a
180 day length of 22.63 (+0.46/-0.45) hours and an average obliquity angle at 22.62
181 (+0.21/-0.21) degree (Table 1). Similarly, Table 1 presents the TimeOptMCMC
182 results for all here analyzed datasets.

183 **The change-point analysis results**

184 In addition, we have integrated our new dataset into the published
185 cyclostratigraphically derived p -values spanning from approximately 200 Ma to 700
186 Ma (Fig. 2). We have also employed change-point analysis (44) (see Methods) to
187 identify the trends of evolution among these reconstructed p -values (Fig. 2). This
188 method has divided these data into three distinct groups which reveal two notable
189 shifts in Earth's rotation deceleration intervals (Fig. 2, *SI Appendix*, Fig. S9). The first
190 substantial shift in Earth's rotation deceleration occurred between ~280 Ma and ~350
191 Ma, representing the first high slope (Fig. 2). The second high slope, indicating
192 another abrupt change in Earth's rotation deceleration, began around ~480 Ma (Fig.
193 2). Specifically, the first group comprises three data points, resulting in a linear
194 deceleration rate of approximately 0.0068 arcsec/Ma. Conversely, the second group,
195 encompassing five data points, does not display a discernible downward trend within
196 this dataset. Finally, the last group, which also consists of five data points, exhibits a
197 pronounced linear downward trend. In this case, we calculate a linear deceleration rate
198 of 0.059 arcsec/Ma, surpassing the rate observed in the first group. Overall, our newly
199 acquired data along with published data suggest a nonlinear staircase variation pattern
200 in Earth's rotation deceleration from 700 Ma to 200 Ma (Fig. 2, *SI Appendix*, Fig. S9).

201 **Discussion**

202 **Comparison of our new geological constraints with tidal models**

203 Previous studies have proposed a series of models to reconstruct the evolution of the
204 Earth-Moon system based on the tidal theory of solid and fluid bodies (6, 10, 13-16,
205 45, 46). While these models provide valuable insights, they vary significantly in the
206 underlying assumptions, constraints, and the approach of obtaining the tidal solution.
207 Consequently, they offer a wide range of possible evolutionary tracks of the Earth-
208 Moon system (Fig. 3b). Therefore, geological observations provide an independent
209 way to constrain the Earth-Moon evolution and test the reliability of these models. In
210 what follows, we compare our new geological findings with five models, namely the
211 La04 (6), W15 (13), T21 (15), D21 (14) and F22 (16) models (Fig. 3).

212 The La04 tidal model is based on the constant time lag assumption (47), where the
213 time it takes the Earth to establish its equilibrium state after the lunar tidal stress is
214 fixed. This assumption is valid when describing the system at present and closely in
215 the past, but fixing the time lag over geological timescales is unjustified given the
216 evolving response of the paleo-oceans. As such, and since the present state of the
217 ocean system corresponds to anomalously high tidal dissipation, the La04 model
218 overestimates the lunar recession rate in the past. Therefore, the Earth's precession
219 frequency in the La04 model shows a higher value in comparison with the rest of the
220 models, as well as the geological records (Fig. 3b). Waltham (13) reconstructed the
221 history of the Earth-Moon separation by employing two fixed endpoints, specifically
222 384 thousand km at the present and approximately 30 thousand km (Roche limit
223 distance) at 4.5 Ga. Clearly, the W15 model reports a higher degree of uncertainty in
224 determining the Earth's precession frequency due to the limited availability of
225 effective constraint parameters. Consequently, nearly all of the geological records
226 align with the Earth's precession frequency ranges depicted in the W15 model, but we
227 note that these data are more concentrated toward the higher end of the range, and
228 those that do not fall within the range are always above it (Fig. 3b).

229 Recent advances in tidal theory, especially for fluid tides, has facilitated the
230 formulation of more refined and physically grounded models. The present state-of-the

231 art models are: T21 (15), D21 (14), and F22 (16) (Fig. 3c). The T21 model adopts a
232 global ocean configuration which persists over the lifetime of the Earth-Moon system,
233 and is parameterized by two free parameters: an effective oceanic thickness and a
234 timescale of tidal dissipation (15). These two parameters were constrained by fitting
235 the reconstructed system history to the geological data available at the time (which
236 mainly correspond to tidal rhythmites and paleontological clocks). Through
237 comparison with the geological data, we have found that the T21 model exhibits a
238 good fit during the past 300 Ma, while beyond 300 Ma, the model results show an
239 increasing discrepancy with geological data (Fig. 3c). In contrast, Daher et al. (14)
240 used a numerical approach to compute the tidal solution by using four different ocean
241 geometry conditions, specifically the present-day (PD) ocean basin geometry and with
242 55 Ma, 116 Ma, and 252 Ma reconstructed basin paleogeometries. The PD continental
243 configuration and mean sea level value result in unusually larger tides both in open-
244 ocean and coastal regions than most periods of geological history (14, 48). Evidently,
245 the D21-PD tidal dissipation rate overestimated the past tidal dissipation, while during
246 600-1000 Ma, the tidal dissipation rate is similar to the PD condition (Fig. 3c). The
247 tidal simulation results for D21-55 and D21-116 exhibit a similar trend to D21-PD but
248 demonstrated a better fit with the geological data for the past 100 Ma (Fig. 3c). The
249 D21-252 tidal simulation underestimates the past tidal dissipation rate, resulting in a
250 longer LOD than geological observations (Fig. 3c). Furthermore, Green et al. (48)
251 also modelled the tidal energy around 252 Ma, and found that the total dissipation
252 rates was much lower than present levels.

253 Recently, Farhat et al. (16) presented a semi-analytical physical tidal model that
254 utilizes two parameters to characterize the ocean: the average ocean depth (H) and a
255 dissipation factor (σ_R). These parameters were tuned such that the reconstructed tidal
256 history fits well with the current tidal recession rates and the Moon's age. While
257 geological data were not incorporated into the model's development, the latter
258 independently aligns well with historical Earth-Moon distance estimations,
259 particularly in concordance with geological constraints derived from

260 cyclostratigraphic techniques (16). Here, we also see a higher degree of similarity
261 between our new p data and previously published geological data, and the F22 tidal
262 model compared to the other theoretical models (Fig. 3). In the F22 model, the Earth-
263 Moon tidal evolution is simulated through three distinct phases, with each phase
264 corresponding to a different ocean model (namely, global and hemispherical oceans)
265 as well as distinct plate tectonic backgrounds since 1 Ga (16). As such, the F22 model
266 took into account the effect of continentality, which was absent in the T21 model, and
267 the effect of evolving surface geometry in a single reconstructed history, which is
268 different from the D21 model. This is probably the potential reason for the better
269 agreement between our geological findings and F22 model.

270 **Staircase patterns of Earth's rotation deceleration**

271 By integrating our new datasets with previously published geological findings, we
272 have observed a notable Earth's rotation deceleration period at 650-500 Ma, which is
273 comparable with the F22 model (Figs. 2, 3b, *SI Appendix*, Fig. S9). During this time
274 interval, the p value experienced a clear reduction from approximately 70 arcsec/yr to
275 around 60 arcsec/yr (Figs. 2, 3b). This deceleration period roughly corresponds to the
276 termination of the Cryogenian glaciations, which may imply that more of Earth's
277 surface was affected by ocean inundation and consequently an intensification in tidal
278 friction (49-51) (*SI Appendix*, Fig. S11b, c, d). During this period, there has been a
279 notable increase in the length of continental arcs, the extent of shallow marine areas
280 and the depth of seawater on continental shelves (*SI Appendix*, Fig. S11b, c, d). The
281 augmented shallow marine regions play a crucial role in governing the tidal
282 dissipation rate since tidal energy dissipation primarily occurs within these areas (14,
283 48).

284 Additionally, during the time period of 500-350 Ma, the new p -values derived from
285 geological data show a relatively stable trend (Fig. 3b). This trend, however, is
286 consistently below the predicted evolution in the F22 model (Fig. 3b). The latter
287 signature could be due to our chosen prior on p ranges from Waltham model (13).
288 Namely, while the staircase pattern is a robust feature of our geological inferences, the

289 absolute position of this pattern on the precession frequency scale is dependent on the
290 chosen prior. Therefore, the fact that the F22-modeled curve lives around the upper
291 limit of our prior distribution can explain the slight offset between the curve and our
292 findings. The gentle trend is located between two high slopes and further validates the
293 staircase shape of the p variations from ~650 Ma to ~280 Ma (Figs. 2, 3b). During this
294 period, we also notice that two p data points (Fig. 3b) derived from Zeeden et al. (31)
295 and Zhong et al. (52) exhibit clear inconsistency with our new geological observations
296 and the F22 tidal model (31, 52). The cyclostratigraphic analysis conducted by Zhong
297 et al. (52) only relies on the main obliquity component ($p+s_3$, s_3 represents the
298 precession of node of the Earth) for calculating the p value. By comparing their result
299 with the tidal models and the majority of geological estimates, their result appears to
300 be inconsistent (31) (Fig. 3b). In order to test the data point of Zeeden et al (31), we
301 compared the variation trends from different datasets (*SI Appendix*, Fig. S9). We have
302 found that although the point of Zeeden et al (31) does not have a clear influence on
303 the trend of 650-500 Ma interval, it has a significant impact on another deceleration
304 period from 350-280 Ma (*SI Appendix*, Fig. S9). Consequently, the data point of
305 Zeeden et al (31) plays a crucial role in constraining the staircase patterns of the
306 Earth's rotation deceleration history from 200 Ma to 700 Ma.

307 In the F22 model (16), there is another deceleration period from 350 Ma to 280 Ma
308 (Fig. 3). For this time interval, the large uncertainty associated with the new
309 geological estimate at 375 Ma in terms of the p -value, coupled with the lack of
310 sufficient geologically-derived p values from this interval, poses a substantial
311 challenge in determining the true trend of the changes on Earth's rotation rate (Fig.
312 3b, *SI Appendix*, Fig. S9). However, if we take account into the data point from
313 Zeeden et al (31), we can nicely recover the evolution of this deceleration period (Fig.
314 2 and *SI Appendix*, Fig. S9). As such, though our dataset provides discrete snapshots
315 of the evolution history at an unprecedented resolution, which are further in good
316 agreement with the F22 model, we maintain the belief that a conclusive and

317 comprehensive description of this interval still requires additional high-quality
318 geological datasets along with improved quantitative analysis methods.

319 **The geological relevance of the Earth's rotation deceleration**

320 The tidal dissipation (1) and Earth dynamic ellipticity (53, 54) are the main driver of
321 changes in the Earth's rotation. Both of them are causally linked to the tectonic and
322 climatic evolution of the Earth. Hence, a correlation between Earth's rotation and
323 some specific geological processes may be anticipated (*SI Appendix*, Figs. S11-S13).
324 Although their interactions are complex and not fully understood, several potential
325 connections have been proposed (2, 47, 55, 56). In this study, the Earth rotation
326 deceleration was accompanied by a rapid increase in the average of Earth's obliquity
327 angle (from $\sim 21.6^\circ$ to $\sim 22.6^\circ$, present day mean obliquity is 23.25°) from ~ 650 Ma to
328 280 Ma (Table 1, *SI Appendix*, Fig. S10). This substantial shift in obliquity may serve
329 as a triggering factor for the development of Earth's glacial periods (e.g., Late
330 Paleozoic Ice Age). In addition, changes in day length (*SI Appendix*, Fig. S10), for
331 instance, can influence the distribution of Solar energy and temperature gradients,
332 potentially impacting weather systems and atmospheric dynamics (57). Interestingly,
333 we also observe that the first oceanic tidal resonance coincides with the
334 Neoproterozoic oxygenation event (NOE, ~ 600 Ma) (58) and the Cambrian explosion
335 (59) (*SI Appendix*, Fig. S12), while the second resonance aligns with both the
336 Phanerozoic oxygenation event (POE, ~ 350 Ma) and late Carboniferous to early
337 Permian biodiversification event (*SI Appendix*, Fig. S12). Therefore, it is important to
338 consider a potential connection between the changes of LOD and the evolution of
339 ocean circulation and ecosystems (56, 60).

340

341 **Methods**

342 **Evaluation and screening of the published cyclostratigraphic datasets**

343 In this study, we have compiled a wide range of cyclostratigraphic time series from
344 published papers (references herein). Firstly, these cyclostratigraphy data are used to
345 estimate the SR based on the independent age model provided in their original text (*SI*

346 *Appendix*, Table S2), thereby establishing a prior hypothesis for the sedimentation
347 rate range used in the following astronomical cycle interpretations, TimeOpt and
348 TimeOptMCMC analysis. Secondly, the Evolutionary Fast Fourier Transform (eFFT)
349 analysis is applied to identify the most significant and stable interval of astronomical
350 cycle signals, with particular emphasis on precession and eccentricity signals.
351 Subsequently, for a promising subselection of case based on the eFFT analyses, the
352 TimeOpt method is employed to investigate the amplitude modulation relationship
353 between precession and eccentricity signals and to determine the optimal
354 sedimentation rate and duration within the chosen interval (*SI Appendix*, Figs. S1-S8).
355 Finally, the decision to perform the TimeOptMCMC analysis is based on the r^2_{opt} and
356 P values obtained from TimeOpt (*SI Appendix*, Table S1).

357

358 **TimeOpt and TimeOptMCMC analysis**

359 Following the approach of ref. (29), all of these selected geological data were firstly
360 tested using the TimeOpt method with prior climatic precession and eccentricity
361 periods to test for an astronomical signal under a relatively wide range of
362 sedimentation rate models. The prior of SR ranges were derived from the original
363 articles (reference herein, *SI Appendix*, Table S2). The statistically significant
364 TimeOpt results (r^2_{opt} , p value; *SI Appendix*, Figs.S1-S8, Table S1) are an important
365 prerequisite for running the MCMC optimization. Bayesian inversion of these
366 geological records are constrained by prior distributions for the fundamental
367 frequencies g_1 to g_5 , the precession frequency p , and SR (*SI Appendix*, Table S2).
368 Prior distributions for the fundamental frequencies g_1 to g_5 are based on the full range
369 of variability in the model simulations of Laskar et al. computed over 500 My (6).
370 The prior distribution for the precession frequency is derived from the study by
371 Waltham (13), which provides a relatively wide range of possibility. Importantly, in
372 this study, we need to note that the different choice of the prior distribution could
373 slightly affect the outcomes of the TimeOptMCMC analysis, but the variation pattern
374 of our datasets is robust, which is independent from the prior distribution. For

375 different cyclostratigraphic datasets, we have run different number of MCMC chains
376 and samples (*SI Appendix*, Table. S1), and then we extracted the post burn-in results
377 of all MCMC chains to calculate the mean value of each parameter with its standard
378 deviation ($\pm\sigma$). For more detailed information about the TimeOpt and
379 TimeOptMCMC methods refer to refs. (29).

380 **Change-point analysis**

381 A changepoint is a sample or time instant at which some statistical property (for
382 instance: mean value, standard deviation, trend) of a signal changes abruptly (44). The
383 MATLAB function ‘findchangepts’ can be used to detect the change points in a time
384 series. We have employed this function to estimate the “linear” statistic properties of
385 the cyclostratigraphically derived p -values time span from 200 Ma to 700 Ma (Fig. 2).
386 To display the abrupt changes on these data, we plot the linear regression lines of
387 different data groups and calculate the mean slope of all regression lines (Fig. 2). In
388 summary, our statistical analysis suggests the presence of two discernible change
389 points/intervals (~280-350 Ma, ~480 Ma) based on these data (Fig. 2; *SI Appendix*,
390 Fig.S9).

391 **Acknowledgments**

392 We thank Zhisong Cao, Hang He and Tianyu Huang for help with performing the
393 TimeOptMCMC and Change-point analyses. We thank Yuyin Li for help with
394 preparing figures and tables. We are grateful for Stephen R. Meyers’ valuable
395 suggestions on our preliminary draft. We thank editors and reviewers for helpful and
396 constructive comments. This work was financially supported by the National Natural
397 Science Foundation of China (grants no. 41888101, 42172137, 42302122, 42050104
398 and 42050102), Sichuan Provincial Youth Science & Technology Innovative
399 Research Group Fund (No. 2022JDTD0004) and European Research Council (ERC)
400 under the European Union’s Horizon 2020 Research and Innovation Program
401 (Advanced Grant AstroGeo-885250). H.H thanks Chengdu University of Technology
402 (CDUT) provides the financial support (Grant No. 21700-000504) for visiting the
403 IMCCE, CNRS, Observatoire de Paris, France. This study is a contribution to the

404 Deep-time Digital Earth (DDE) Big Science Program. Moreover, this study benefited
405 from the researchers who made their research code (Astrochron software; Meyers,
406 2014) and original data accessible.

407 **References**

- 408 1. G.A. Darwin, A tidal theory of the evolution of satellites. *Observatory* 3, 79–84
409 (1879).
410
- 411 2. C. M. G. Pannella, M. N. Thompson, 1968. Paleontological Evidence of Variations
412 in Length of Synodic Month since Late Cambrian. *Science*. 162, 792-796 (1968).
413
- 414 3. B.G. Bills, R.D. Ray, Lunar orbital evolution: A synthesis of recent results.
415 *Geophysical Research Letters*. 26, 3045-3048 (1999).
416
- 417 4. E.P. Kvale, H.W. Johnson, C.P. Sonett, A.W. Archer, A. Zawistoski, Calculating
418 lunar retreat rates using tidal rhythmites. *Journal of Sedimentary Research*. 69,
419 1154-1168 (1999).
420
- 421 5. G. E. Williams, Geological Constraints on the Precambrian History of Earth's
422 Rotation and the Moon's Orbit. *Rev. Geophys.* 38, 37–59 (2000).
423
- 424 6. J. Laskar, P. Robute, F. Joutel, M. Gastineau, A. C. M. Correia, and B. Levrard, A
425 long-term numerical solution for the insolation quantities of the Earth. *Astron.*
426 *Astrophys.* 428, 261–285 (2004).
427
- 428 7. J.G.Williams, D.H. Boggs, Secular tidal changes in lunar orbit and Earth rotation.
429 *Celest. Mech. Dyn. Astron.* 126, 89–129 (2016).
430
- 431 8. M. Maurice, N. Tosi, S. Schwinger, D. Breuer, T. Kleine, A long-lived magma
432 ocean on a young Moon. *Sci. Adv.*, 6, eaba8949 (2020).
433
- 434 9. H. Gerstenkorn, On the controversy over the effect of tidal friction upon the history
435 of the earth-moon system. *Icarus*, 7, 160–167 (1967).
436
- 437 10. J. Webb, Tides and the evolution of the Earth-Moon system. *Geophys. J. R. Astron.*
438 *Soc.* 70, 261–271 (1982).
439

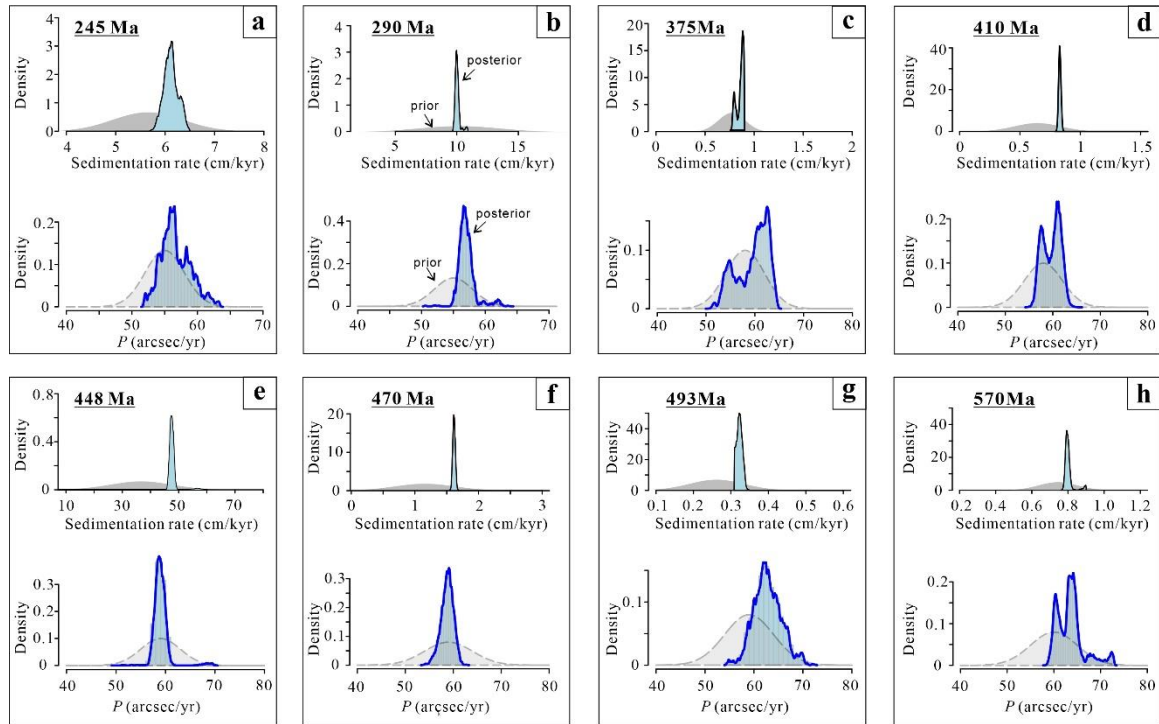
- 440 11. F. Tera and G.J. Wasserburg, U-Th-Pb systematics in lunar highland samples from
441 the Luna 20 and Apollo 16 missions. *Earth and Planetary Science Letters*, 17, 36-
442 51 (1972).
443
- 444 12. M. Barboni, P. Boehnke, B. Keller et al., Early formation of the Moon 4.51 billion
445 years ago. *Sci. Adv.*, 3, e1602365 (2017).
446
- 447 13. D. Waltham, Milankovitch period uncertainties and their impact on
448 cyclostratigraphy. *J. Sediment. Res.* 85, 990–998 (2015).
449
- 450 14. H. Daher et al., Long-term Earth-Moon evolution with high-level orbit and ocean
451 tide models. *J. Geophys. Res. Planets.* 126, e2021JE006875 (2021).
452
- 453 15. R. H. Tyler, On the tidal history and future of the Earth–Moon orbital system. *Plan.*
454 *Sci. J.* 2, 70 (2021).
455
- 456 16. M. Farhat, P. Auclair-Desrotour, G. Boue, J. Laskar, The resonant tidal evolution
457 of the Earth-Moon distance. *Astron. Astrophys.* 665, L1 (2022).
458
- 459 17. C. P. Sonett, M. A. Chan, Neoproterozoic Earth-Moon dynamics: Rework of the
460 900 Ma Big Cottonwood Canyon tidal laminae. *Geophysical Research Letters*, 25,
461 539–542, (1998).
462
- 463 18. T. Eulendorf and C. Heubeck, Constraints on Moon’s Orbit 3.2 billion years ago
464 from tidal bundle data. *Journal of Geophysical Research: Planets.* 128,
465 e2022JE007466 (2023).
466
- 467 19. J. W. Wells, Coral growth and geochronometry. *Nature.* 197, 948-950 (1963).
468
- 469 20. K. Lambeck, *The Earth’s Variable Rotation* (Cambridge University Press, 1980).
470
- 471 21. J. P. Vanyo, S. M. Awramik, Stromatolites and Earth–Sun–Moon dynamics.
472 *Precambrian Research*, 29, 121–142 (1985).
473
- 474 22. N.J. de Winter, S. Goderis, V. Malderen, M. Sinnesael, S. Vansteenberge, C.
475 Snoeck, J. Belza, F. Vanhaecke, P. Claeys, Subdaily-Scale Chemical Variability in
476 a *Torreites Sanchezi* Rudist Shell: Implications for Rudist Paleobiology and the
477 Cretaceous Day-Night Cycle. *Paleoceanography and Paleoclimatology.* 35 (2020).
478

- 479 23. S. D. Deines, C. A. Williams, Earth's Rotational Deceleration: Determination of
480 Tidal Friction Independent of Timescales. *The Astronomical Journal*. 151, 103
481 (2016).
482
- 483 24. J. Laskar, M. Farhat, M. Lantink, P. auclair-Desrotour, G. Bou'e, M. Sinnesael, Did
484 atmospheric thermal tides cause a daylength locking in the Precambrian? A review
485 on recent results. arXiv:2309.11479 (2023).
486 <https://doi.org/10.48550/arXiv.2309.11479>
487
- 488 25. C. Heubeck, S. Biasing, M. Grund, N. Drabon, M. Homann, S. Nabhan, Geological
489 constraints on Archean (3.22 Ga) coastal-zone processes from the Dycedale
490 Syncline, Barberton Greenstone Belt. *South Afr. J. Geol.*, 119, 495–518 (2016).
491
- 492 26. J. C. Walker, K. J. Zahnle, Lunar nodal tide and distance to the Moon during the
493 Precambrian. *Nature*, 320, 600-602 (1986).
494
495
- 496 27. C. P. Sonett, E. P. Kvale, A. Zakharian, M. A. Chan, T. M. Demko, Late Proterozoic
497 and Paleozoic tides, retreat of the Moon, and rotation of the Earth. *Science*,
498 273(5271), 100-104 (1996).
499
- 500 28. G. E. Williams, Precambrian length of day and the validity of tidal rhythmite
501 paleotidal values. *Geophysical Research Letters*, 24(4), 421-424(1997).
502
- 503 29. S. R. Meyers, A. Malinverno, Proterozoic Milankovitch cycles and the history of
504 the solar system. *Proc. Natl. Acad. Sci. U.S.A.* 115, 6363–6368 (2018).
505
- 506 30. M. L. Lantink, J. Davies, M. Ovtcharova, F. J. Hilgen, Milankovitch cycles in
507 banded iron formations constrain the Earth-Moon system 2.46 billion years ago.
508 *Proc Natl Acad Sci U.S.A.* 119, e2117146119 (2022).
509
- 510 31. C. Zeeden, J. Laskar, D. V Vleeschouwer, D. Pas, A.C. Da Silva, Earth's rotation
511 and Earth-Moon distance in the Devonian derived from multiple geological records.
512 *Earth Planet. Sci. Lett.* 621, 118348 (2023).
513
- 514 32. H. Huang, Y. Gao, M. M. Jones, H. Tao, A. R. Carroll, D. E. Ibarra, H. Wu, C.
515 Wang, Astronomical forcing of Middle Permian terrestrial climate recorded in a
516 large paleolake in northwestern China. *Palaeogeography, Palaeoclimatology,*
517 *Palaeoecology.* 550, 109735 (2020).
518
- 519 33. T. Zhang, Y. Li, T. Fan, A. C. Da Silva, J. Shi, Q. Gao, M. Kuang, W. Liu, Z. Gao,
520 M. Li, Orbitally-paced climate change in the early Cambrian and its implications

- 521 for the history of the Solar System. *Earth Planet. Sci. Lett.* 583, 117420 (2022).
522
- 523 34. M. Zhou, H. Wu, L. A. Hinnov, Q. Fang, S. Zhang, T. Yang, M. Shi, Empirical
524 Reconstruction of Earth-Moon and Solar System Dynamical Parameters for the
525 Past 2.5 Billion Years From Cyclostratigraphy. *Geophysical Research Letters*. 49
526 (2022).
527
- 528 35. D. De Vleeschouwer, D. E. Penman, S. D’Haenens, F. Wu, T. Westerhold, M.
529 Vahlenkamp, C. Cappelli, C. Agnini, W.E.C. Kordesch, D.J. King, R. van der Ploeg,
530 H. Pälike, S. K. Turner, P. Wilson, R. D. Norris, J. C. Zachos, S. M. Bohaty, P. M.
531 Hull, North Atlantic Drift Sediments Constrain Eocene Tidal Dissipation and the
532 Evolution of the Earth-Moon System. *Paleoceanography and Paleoclimatology*. 38
533 (2023).
534
- 535 36. K. J. Zahnle, J. C. G. Walker, A constant daylength during the Precambrian era?
536 *Precambrian Res*, 37: 95-105 (1987).
537
- 538 37. M. Li, C. Huang, L. Hinnov, W. Chen, J. Ogg, W. Tian, Astrochronology of the
539 Anisian stage (Middle Triassic) at the Guandao reference section, South China.
540 *Earth Planet. Sci. Lett.*,482, 591-606 (2018).
541
- 542 38. D. De Vleeschouwer, A.C. Da Silva, M. Sinnesael, D. Chen, J.E. Day, M.T. Whalen,
543 Z. Guo, P. Claeys, Timing and pacing of the Late Devonian mass extinction event
544 regulated by eccentricity and obliquity. *Nature Communications*. 8 (2017).
545
- 546 39. A.C. Da Silva, J. Hladil, L. Chadimová, L. Slavík, F.J. Hilgen, O. Bábek, M.J.
547 Dekkers, Refining the Early Devonian time scale using Milankovitch cyclicality in
548 Lochkovian–Pragian sediments (Prague Synform, Czech Republic). *Earth and
549 Planetary Science Letters*. 455, 125-139 (2016).
550
- 551 40. M. Sinnesael, P.I. McLaughlin, A. Desrochers, A. Mauviel, J. De Weirtdt, P. Claeys,
552 T.R.A. Vandenbroucke, Precession-driven climate cycles and time scale prior to
553 the Hirnantian glacial maximum. *Geology* (2021).
554
- 555 41. K. Ma, R. Li, L.A. Hinnov, Y. Gong, Conodont biostratigraphy and astronomical
556 tuning of the Lower-Middle Ordovician Liangjiashan (North China) and
557 Huanghuachang (South China) marine sections. *Palaeogeography
558 Palaeoclimatology Palaeoecology*. 528, 272-287 (2019).
559
- 560 42. A. L. Sørensen, A. T. Nielsen, N. Thibault, Z. Zhao, N.Schovsbo, T. W. Dahl,

- 561 Astronomically forced climate change in the late Cambrian. *Earth Planet. Sci. Lett.*
562 548, 116475 (2020).
563
- 564 43. H. Li, S. Zhang, J. Han, T. Zhong, J. Ding, H. Wu, P. Liu, J. Dong, Z. Zhang, T.
565 Yang, G. Jiang, Astrochronologic calibration of the Shuram carbon isotope
566 excursion with new data from South China. *Global and Planetary Change.* 209,
567 103749 (2022).
568
- 569 44. Killick, R., Eckley, I. A., changepoint: An R Package for Change-point Analysis.
570 *Journal of Statistical Software.* 58 (3), 1-19 (2014).
571
- 572 45. K. S. Hansen, Secular effects of oceanic tidal dissipation on the Moon's orbit and
573 the Earth's rotation. *Rev. Geophys. Space Phys.* 20, 457–480 (1982).
574
- 575 46. A. Berger, M. F. Loutre, J. Laskar, Stability of the astronomical frequencies over
576 the Earth's history for paleoclimate studies. *Science* 255, 560–566 (1992).
577
- 578 47. F. Mignard, The evolution of the lunar orbit revisited. I. The Moon and the planets,
579 20(3), 301-315 (1979).
580
- 581 48. J. A. M. Green, M. Huber, D. Waltham, J. Buzan, M. Wells, Explicitly modelled
582 deep-time tidal dissipation and its implication for Lunar history. *Earth Planet. Sci.*
583 *Lett.* 461, 46–53 (2017).
584
- 585 49. W. Cao, C. T. A. Lee, J.S. Lackey, Episodic nature of continental arc activity since
586 750 Ma: a global compilation. *Earth Planet. Sci. Lett.* 461, 85–95 (2017).
587
- 588 50. S.E. Peter and J.M. Husson, Sediment cycling on continental and oceanic crust.
589 *Geology* (2016).
590
- 591 51. R.D. Nance, J.B. Murphy, M. Santosh, The supercontinent cycle: A retrospective
592 essay. *Gondwana Research.* 25, 4-29 (2014).
593
- 594 52. Y. Zhong, H. Wu, J. Fan, Q. Fang, M. Shi, S. Zhang, T. Yang, H. Li, L. Cao, Late
595 Ordovician obliquity-forced glacio-eustasy recorded in the Yangtze Block, South
596 China. *Palaeogeogr. Palaeoclimatol. Palaeoecol.*, 540, 109520 (2020).
597
- 598 53. L. J. Lourens, R. Wehausen, H. J. Brumsack, Geological constraints on tidal
599 dissipation and dynamical ellipticity of the Earth over the past three million years.

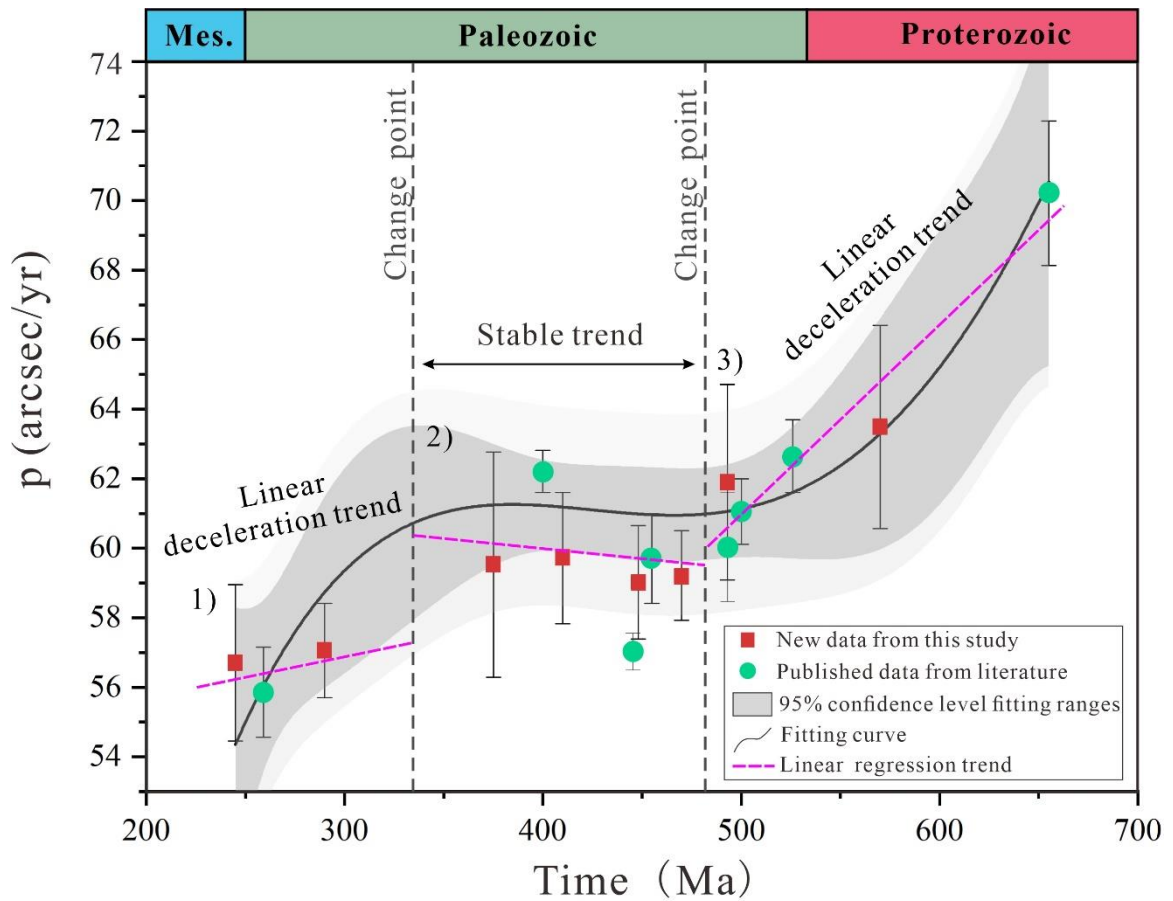
- 600 Nature, 409(6823), 1029-1033 (2001).
601
- 602 54. M. Farhat, J. Laskar, G. Boué, Constraining the Earth's Dynamical Ellipticity From
603 Ice Age Dynamics. *Journal of Geophysical Research: Solid Earth*, 127, 1-22 (2022).
604
- 605 55. W.R. Peltier, Postglacial variations in the level of the sea: Implications for climate
606 dynamics and solid-Earth geophysics. *Reviews of Geophysics*. 36, 603-689 (1998).
607
- 608 56. J. M. Klatt, A. Chennu, B. K. Arbic, B. A. Biddanda, G. J. Dick, Possible link
609 between Earth's rotation rate and oxygenation. *Nat. Geosci.* 14, 564-570 (2021).
610
- 611 57. S.J. Gregory, G.M. Hal, W.R. Kuhn, Precambrian Climate: The Effects of Land
612 Area and Earth's Rotation Rate. *J. Geophys. Res.* 98, 8785-8791 (1993).
613
- 614 58. T.W. Lyons, C.T. Reinhard, N.J. Planavsky, The rise of oxygen in Earth's early
615 ocean and atmosphere. *Nature*. 506, 307-315 (2014).
616
- 617 59. J. Fan, S. Shen, D.H. Erwin, P.M. Sadler, N. MacLeod, Q. Cheng, X. Hou, J. Yang,
618 X. Wang, Y. Wang, H. Zhang, X. Chen, G. Li, Y. Zhang, Y. Shi, D. Yuan, Q. Chen,
619 L. Zhang, C. Li, Y. Zhao, A high-resolution summary of Cambrian to Early Triassic
620 marine invertebrate biodiversity. *Science*. 367, 272-277 (2020).
621
- 622 60. M. Green, D. Hadley-Pryce, C. Scotese, A journey through tides: Phanerozoic (541
623 Ma-present day). 157-184 (2023).
624
- 625
- 626



629

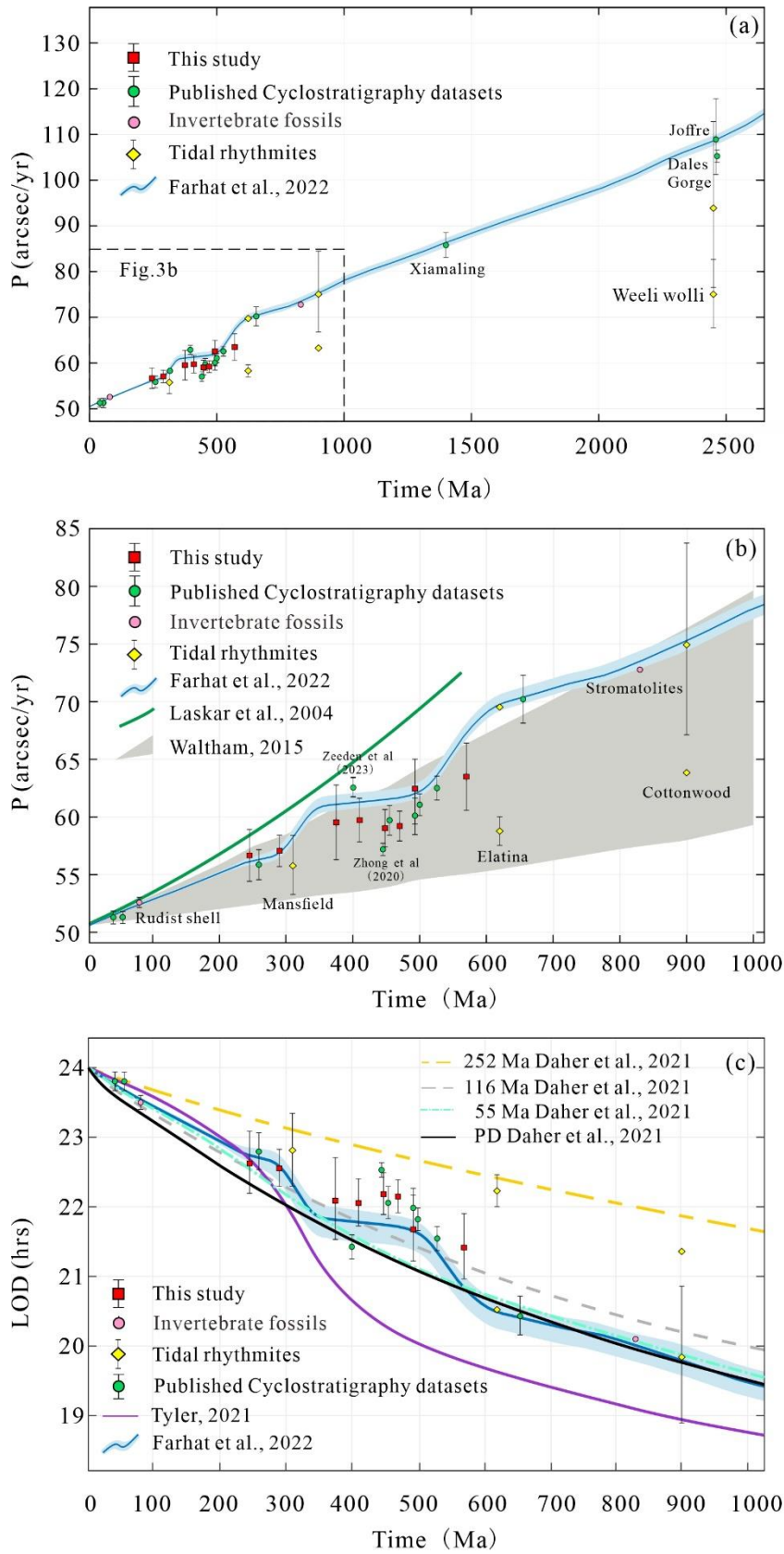
630 **Figure 1. Prior and posterior distributions of the SR and p .** (a). The cyclostratigraphic
 631 record from ref. (37) at 245 Ma and the TimeOptMMC analysis reveals a prominent SR of
 632 6.12 ± 0.14 cm/kyr, while the distribution of p values is at 56.70 ± 2.26 arcsec/yr. (b). The
 633 cyclostratigraphic record obtained from ref. (32) at 290 Ma indicates a notable SR of
 634 10.04 ± 0.20 cm/kyr, as revealed by the TimeOptMMC analysis. Additionally, the distribution
 635 of p values is observed to be at 57.06 ± 1.36 arcsec/yr. (c). The cyclostratigraphic record from
 636 ref. (38) at 375 Ma reveals a significant SR of 0.81 ± 0.04 cm/kyr, and the distribution of p
 637 values is observed to be 59.53 ± 3.24 arcsec/yr. (d). The cyclostratigraphic record from ref.
 638 (39) at 410 Ma reveals a significant SR of 0.83 ± 0.01 cm/kyr, and the distribution of p values
 639 is observed to be 59.72 ± 1.89 arcsec/yr. (e). The cyclostratigraphic record from ref. (40) at 448
 640 Ma reveals a significant SR of 47.74 ± 1.51 cm/kyr, and the distribution of p values is observed
 641 to be 59.02 ± 1.63 arcsec/yr. (f). The cyclostratigraphic record from ref. (41) at 470 Ma reveals
 642 a significant SR of 1.61 ± 0.02 cm/kyr, and the distribution of p values is observed to be
 643 59.21 ± 1.29 arcsec/yr. (g). The cyclostratigraphic record obtained from ref. (42) at 493 Ma
 644 reveals a significant SR of 0.34 ± 0.008 cm/kyr, as determined by the TimeOptMMC analysis.
 645 Furthermore, the distribution of p values is observed to be at 62.76 ± 2.81 arcsec/yr. (h). The
 646 cyclostratigraphic record from ref. (43) at 570 Ma and the TimeOptMMC analysis reveals a
 647 prominent SR of 0.80 ± 0.02 cm/kyr, while the distribution of p values is at 63.49 ± 2.92
 648 arcsec/yr. Shaded grey areas indicate the prior distributions, and blue-shaded histograms
 649 indicate the posterior distributions obtained by the Markov Chain Monte Carlo sampling.

650



651

652 **Figure 2. The cyclostratigraphic-reconstructed Earth's precession frequencies and**
 653 **their trends.** The grey shaded area indicates the 95% confidence level for the fitted data range.
 654 The black curve represents the polynomial fitting results for these data. The black dotted lines
 655 represent the outputs of the change-point analysis, which have divided the data into three groups.
 656 The purple dotted curves represent the linear regression trends for the data points within each of
 657 the three groups. Mes: Mesozoic.



658

659

660 **Figure 3. Comparison of p , LOD with tidal model predictions.** (a). The estimated Earth
 661 precession frequency versus the F22 tidal model (16). (b). The estimated Earth precession

662 frequency versus the astronomical models, the green line shows Laskar's model (Eq (40) in
663 ref. (6)), the blue curve with narrow error range was cited from ref. (16), the grey area
664 delineates the error range given by Waltham's model (13). (c). Comparison of the
665 reconstructed LOD with tidal model results, the tidal models are from the refs. (14-16). Note:
666 the D21 model (14) has calculated four tidal evolution solutions based on present-day (PD)
667 ocean basin geometry and with 55 Ma, 116 Ma, and 252 Ma reconstructed basin
668 paleogeometries. The red square points with error bars are results in this study, the green
669 circle points with error bars data are from published cyclostratigraphic articles, the purple and
670 yellow data points originated from the invertebrate fossils and tidal rhythmites, respectively.

671

672 **Table 1.** The TimeOptMCMC reconstruction results of the cyclostratigraphic records in this
673 study.

674

Time (Ma)	p (arcsec/yr)	EMD (1000 km)	LOD (hrs)	Obliquity (°)
245	56.70±2.26	373.99 (+3.36/-3.22)	22.63 (+0.46/-0.45)	22.62 (+0.21/-0.21)
290	57.06±1.36	373.47 (+1.99/-1.95)	22.55 (+0.28/-0.26)	22.58 (+0.13/-0.12)
375	59.53±3.24	369.96 (+4.63/-4.39)	22.09 (+0.62/-0.56)	22.36 (+0.29/-0.27)
410	59.72±1.89	369.69 (+2.67/-2.58)	22.05 (+0.36/-0.33)	22.35 (+0.16/-0.16)
448	59.02±1.63	370.67 (+2.32/-2.26)	22.18 (+0.31/-0.29)	22.41 (+0.14/-0.14)
470	59.21±1.29	370.40 (+1.83/-1.78)	22.15 (+0.24/-0.23)	22.39 (+0.11/-0.11)
493	62.76±2.81	365.58 (+3.79/-3.63)	21.53 (+0.48/-0.44)	22.16 (+0.24/-0.22)
570	63.49±2.92	364.62 (+3.90/-3.73)	21.41 (+0.49/-0.45)	22.04 (+0.23/-0.23)

675 Note: EMD represents the Earth-Moon distance; LOD indicates the length of the solar day.
676 The uncertainty of these values are based on 1 δ standard deviation.

677

678

679

Supporting Information for:

680

Geological evidence confirms the staircase patterns of Earth's

681

rotation deceleration from the Neoproterozoic to the Mesozoic Era

682

He Huang^{1,2,3}, Chao Ma^{1,2,*}, Jacques Laskar³, Matthias Sinnesael³, Mohammad

683

Farhat³, Nam H. Hoang³, Yuan Gao⁴, Christian Zeeden⁵, Hanting Zhong^{1,2}, Mingcai

684

Hou^{1,2}, Chengshan Wang⁴

685

¹ State Key Laboratory of Oil and Gas Reservoir Geology and Exploitation, Institute of

686

Sedimentary Geology, Chengdu University of Technology, Chengdu 610059, China

687

² Key Laboratory of Deep-time Geography and Environment Reconstruction and Applications

688

of Ministry of Natural Resources, Chengdu University of Technology, Chengdu 610059,

689

China

690

³ IMCCE, CNRS, Observatoire de Paris, PSL University, Sorbonne Université, 75014, Paris,

691

France

692

⁴ State Key Laboratory of Biogeology and Environmental Geology, China University of

693

Geosciences (Beijing), Beijing 100083, China

694

⁵ LIAG-Leibniz Institute for Applied Geophysics, Stilleweg 2, 30655 Hannover, Germany

695

696

Corresponding author: Chao Ma

697

Email: machao@cdut.edu.cn

698

699

This PDF file includes:

700

Tables S1 to S2

701

Figures S1 to S13

702

Supplementary R scripts

703

SI References

704

The paper is a non-peer reviewed preprint submitted to EarthArXiv

705

706 **Supplementary Tables**

707

708 **Table S1.** The detailed information of the geological data in this study. We also provided some of the key parameters for running the TimeOpt and
 709 TimeOptMCMC analysis.

Epoch/Era	Time (Ma)	Formation /Location/ Fossil	Proxy	TimeOpt r^2_{opt} value	TimeOptMCMC Num. of samples and chains	P (arcsec/yr)	$\pm\sigma$ (arcsec/yr)	Data Resource
Today*	0 Ma					50.475838		ref. (6)
Eocene [§]	41 Ma	Newfoundland Ridge	Ca/Fe			51.28	0.56	ref. (35)
Eocene [§]	55 Ma	Walvis Ridge	a*(red/green)	0.212	200,000; 150	51.28	0.52	ref. (29)
Campanian [†]	80 Ma	Rudist Shell	XRF			52.58	0.44	ref. (22)
Anisian	245 Ma	Guandao	GR	0.207	200,000; 100	56.70	2.26	ref. (37)
Wuchiapingian [§]	259 Ma	Wujiaping	ARM	0.246	600,000; 50	55.86	1.30	ref. (34)
Artinskian	290 Ma	Lucaogou	GR	0.199	100,000; 150	57.06	1.36	ref. (32)
Frasnian	375 Ma	H-32, Iowa	MS	0.19	100,000; 200	59.53	3.24	ref. (38)
Emsian [§]	~400 Ma		MS			62.61	0.60	ref. (31)
Pragian	410 Ma	Požár-CS	MS	0.162	200,000; 150	59.72	1.89	ref. (39)
Katian	448 Ma	Anticosti Island	K%	0.215	200,000; 100	59.02	1.63	ref. (40)
Sandbian [§]	455 Ma	Pingliang	MS	0.094	1,000,000; 30	59.71	1.29	ref. (34)
Floian	470 Ma	Liangjiashan	Ca%	0.121	600,000; 50	59.21	1.29	ref. (41)
Jiangshanian	493 Ma	Alum Shale	S%	0.184	200,000; 100	62.76	2.81	ref. (42)
Cambrian [§]	500 Ma	Luoyixi section	MS			61.06	0.94	ref. (64)
Cambrian [§]	526 Ma	Qiongzhusi	Fe/Al			62.65	1.04	ref. (33)
Ediacaran	570 Ma	Doushantuo	MS	0.189	200,000; 100	63.49	2.92	ref. (43)
Cryogenian [§]	655 Ma	Datangpo	MS	0.215	1,000,000; 30	70.21	2.08	ref. (34)
Tonian [†]	830 Ma	Stromatolites				72.77	/	ref. (21)
Tonian [†]	900 Ma	Tidal laminae				74.9	+8.85/- 7.78	ref. (17)

Mesoproterozoic [§]	1400 Ma	Xiamaling	Cu/Al	0.3	1,000,000; 50	85.79	1.36	ref. (29)
Paleoproterozoic [§]	2460 Ma	Joffre	Lithological index			108.6	8.5	ref. (30)
Paleoproterozoic [§]	2465 Ma	Dales Gorge	Greyscale	0.087	1,000,000; 30	105.26	1.35	ref. (34)

710 *Earth's rotation rate estimates from ref. (6).

711 [§]Earth's rotation results inferred from cyclostratigraphic analysis from the published articles.

712 [†]Earth's rotation results calculated from the tidalites and/or invertebrate fossil growth cycle from the published articles.

713 Note: All the errors in this table are one standard deviation ($\pm\sigma$), the bold terms in this table are calculated by this study.

714 GR: gamma ray; ARM: anhysteretic remanent magnetization; MS: magnetic susceptibility.

715

716

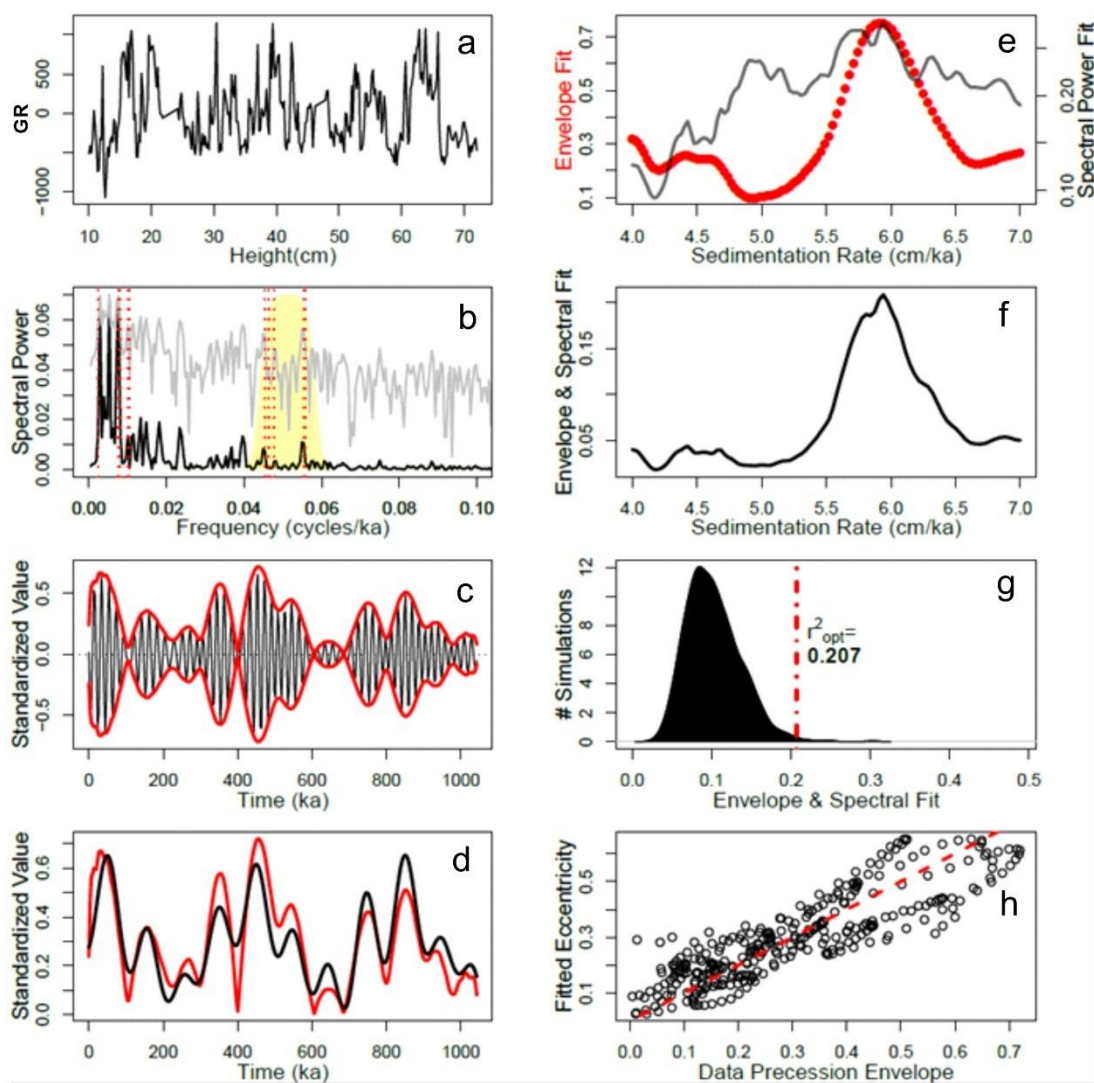
717 **Table S2.** Definition of TimeOptMCMC priors for sedimentation rate, Earth axial precession
 718 frequency p and secular frequency g_i terms.

Time (Ma)	Sedimentary rate (cm/kyr)	P (arcsec/yr)	g_i terms (arcsec/yr)
245	4-7 (ref. 37)	54.5 ± 2.5	
290	2-18 (ref. 32)	55 ± 3	$g_1=5.525 \pm 0.125$
375	0.7-1 (ref. 38)	58 ± 4	$g_2=7.455 \pm 0.015$
410	0.2-1(ref. 39)	58 ± 4	$g_3=17.3 \pm 0.15$
448	10-60 (ref. 40)	59 ± 4	$g_4=17.85 \pm 0.15$
470	0.1-1.8 (ref. 41)	59 ± 5	$g_5=4.257455 \pm 0.00002$
493	0.1-0.4 (ref.42)	59 ± 5	
570	0.5-0.9 (ref.43)	60 ± 5	

719 Note: Prior distributions for the fundamental frequencies g_1 to g_5 are based on the full range of
 720 variability in the model simulations of ref. (6) computed over 500 My. The prior distribution for
 721 the precession frequency is derived from the recent study by ref. (13).

722

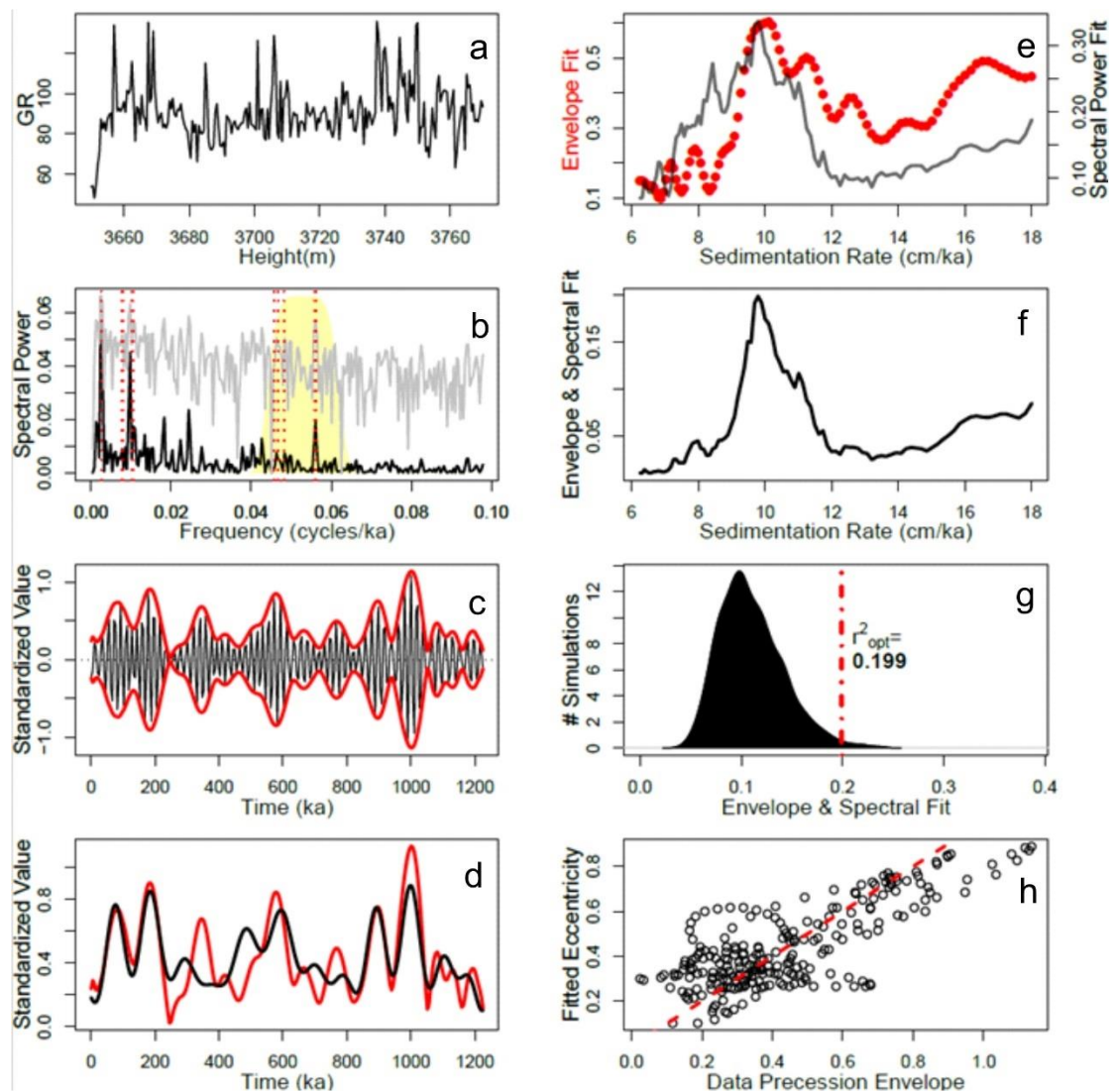
723



725

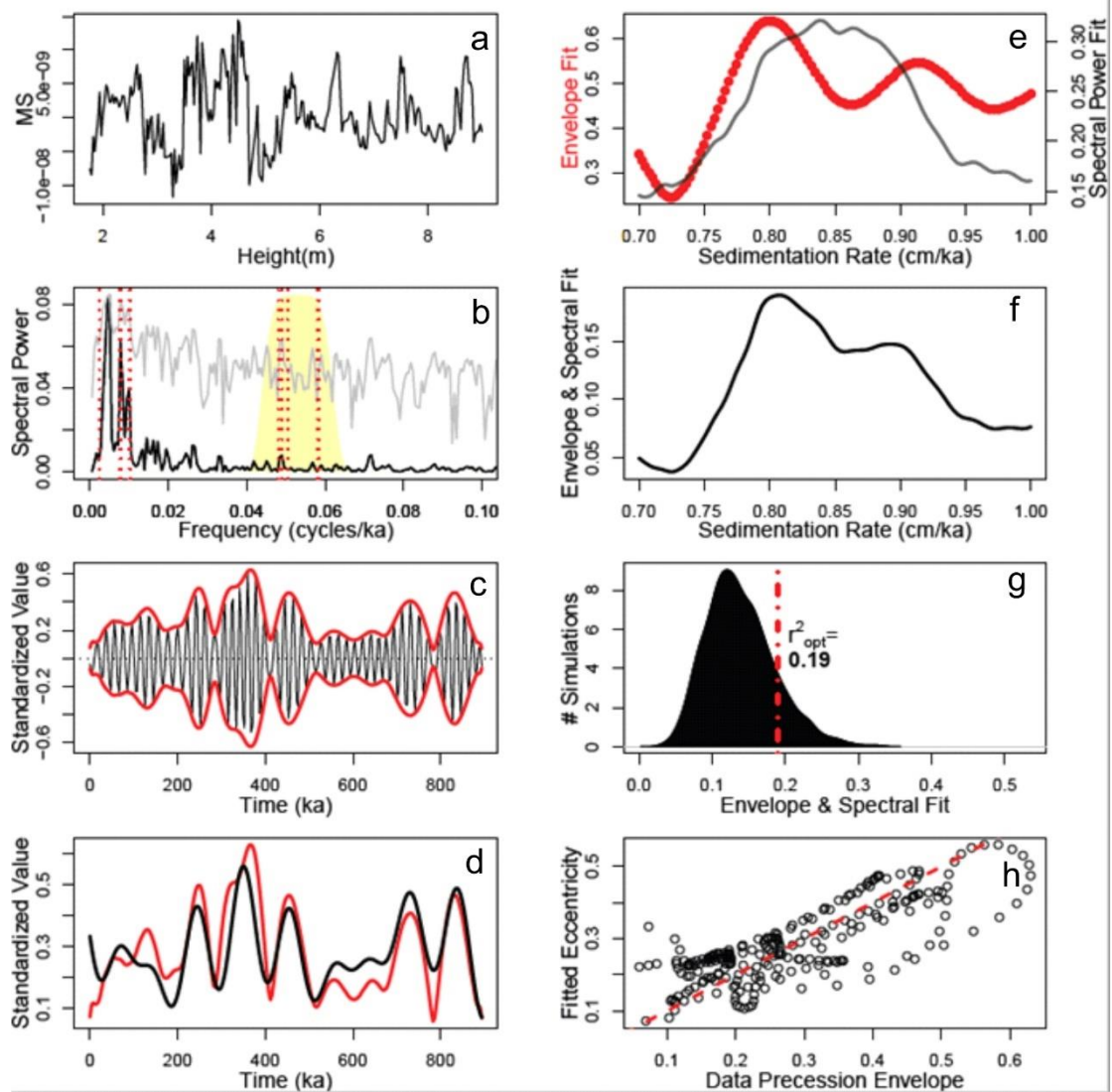
726 **Figure S1.** TimeOpt analysis of the GR data from the Guandao section. (a) The GR data of
 727 Guandao section (37). (b) Periodogram for the GR data (black line=linear spectrum; gray
 728 line=log spectrum). Yellow shaded region indicates the portion of the spectrum bandpass
 729 filtered for evaluation of the precession amplitude envelope. Vertical dashed red lines indicate
 730 the eccentricity and climatic precession target periods. (c) Extracting the band-passed
 731 precession signal (black), and the data amplitude envelope (red) determined via Hilbert
 732 transform. (d) Comparison of the data amplitude envelope (red) and the TimeOpt reconstructed
 733 eccentricity model (black). (e) Squared Pearson correlation coefficient for the amplitude
 734 envelope fit and the spectral power fit as a function of sedimentation rate. (f) Combined
 735 envelope and spectral power fit at each evaluated sedimentation rate. (g) Summary of 2000
 736 Monte Carlo simulations with AR1 surrogates. (h) Cross plot of the data amplitude envelope
 737 and the TimeOpt-reconstructed eccentricity model in panel “d”; dashed red line is the 1:1 line.

738



739

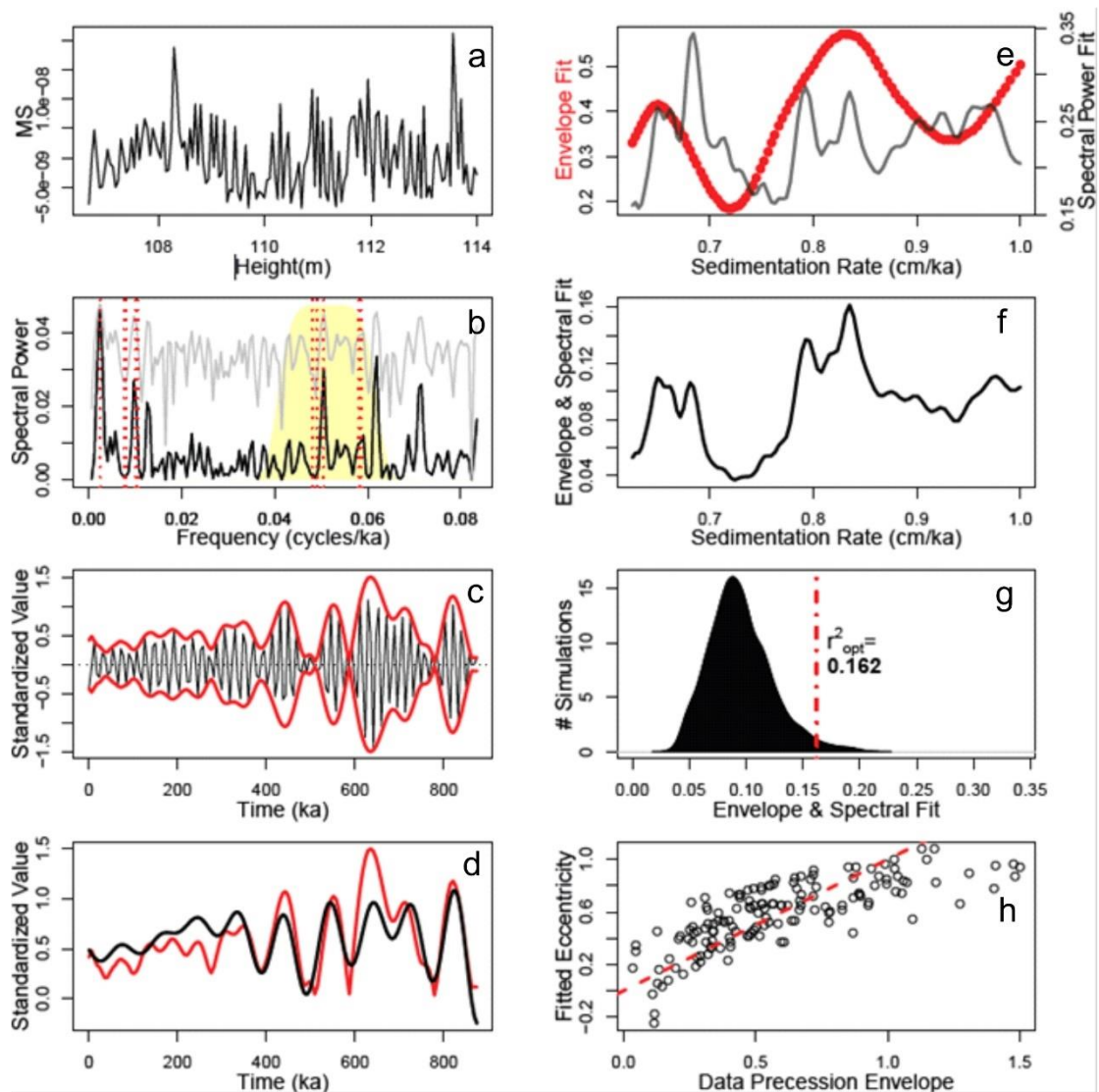
740 **Figure S2.** TimeOpt analysis of the GR series from the Lucaogou Formation. (a) The GR data
 741 of Ji251 well (32), which geological age was recalibrated by ref. (61). (b) Periodogram for the
 742 GR data, given the TimeOpt derived sedimentation rate of 9-10 cm/kyr (black line=linear
 743 spectrum; gray line=log spectrum). Yellow shaded region indicates the portion of the
 744 spectrum bandpassed for evaluation of the precession amplitude envelope. Vertical dashed
 745 red line indicate the eccentricity and climatic precession target periods. (c) Extracting the
 746 band-passed precession signal (black), and the data amplitude envelope (red) determined via
 747 Hilbert transform. (d) Comparison of the data amplitude envelope (red) and the TimeOpt
 748 reconstructed eccentricity model (black). (e) Squared Pearson correlation coefficient for the
 749 amplitude envelope fit and the spectral power fit as a function of sedimentation rate. (f)
 750 Combined envelope and spectral power fit at each evaluated sedimentation rate. (g) Summary
 751 of 2000 Monte Carlo simulations with AR1 surrogates. (h) Cross plot of the data amplitude
 752 envelope and the TimeOpt-reconstructed eccentricity model in panel “d”; dashed red line is
 753 the 1:1 line.



754

755 **Figure S3.** TimeOpt analysis of the MS series from the H-32 core. (a) The MS data of H-32
 756 core (38). (b) Periodogram for the MS data (black line=linear spectrum; gray line=log
 757 spectrum). Yellow shaded region indicates the portion of the spectrum bandpassed for
 758 evaluation of the precession amplitude envelope. Vertical dashed red line indicate the
 759 eccentricity and climatic precession target periods. (c) Extracting the band-passed precession
 760 signal (black), and the data amplitude envelope (red) determined via Hilbert transform. (d)
 761 Comparison of the data amplitude envelope (red) and the TimeOpt reconstructed eccentricity
 762 model (black). (e) Squared Pearson correlation coefficient for the amplitude envelope fit and
 763 the spectral power fit as a function of sedimentation rate. (f) Combined envelope and spectral
 764 power fit at each evaluated sedimentation rate. (g) Summary of 2000 Monte Carlo simulations
 765 with AR1 surrogates. (h) Cross plot of the data amplitude envelope and the TimeOpt-
 766 reconstructed eccentricity model in panel “d”; dashed red line is the 1:1 line.

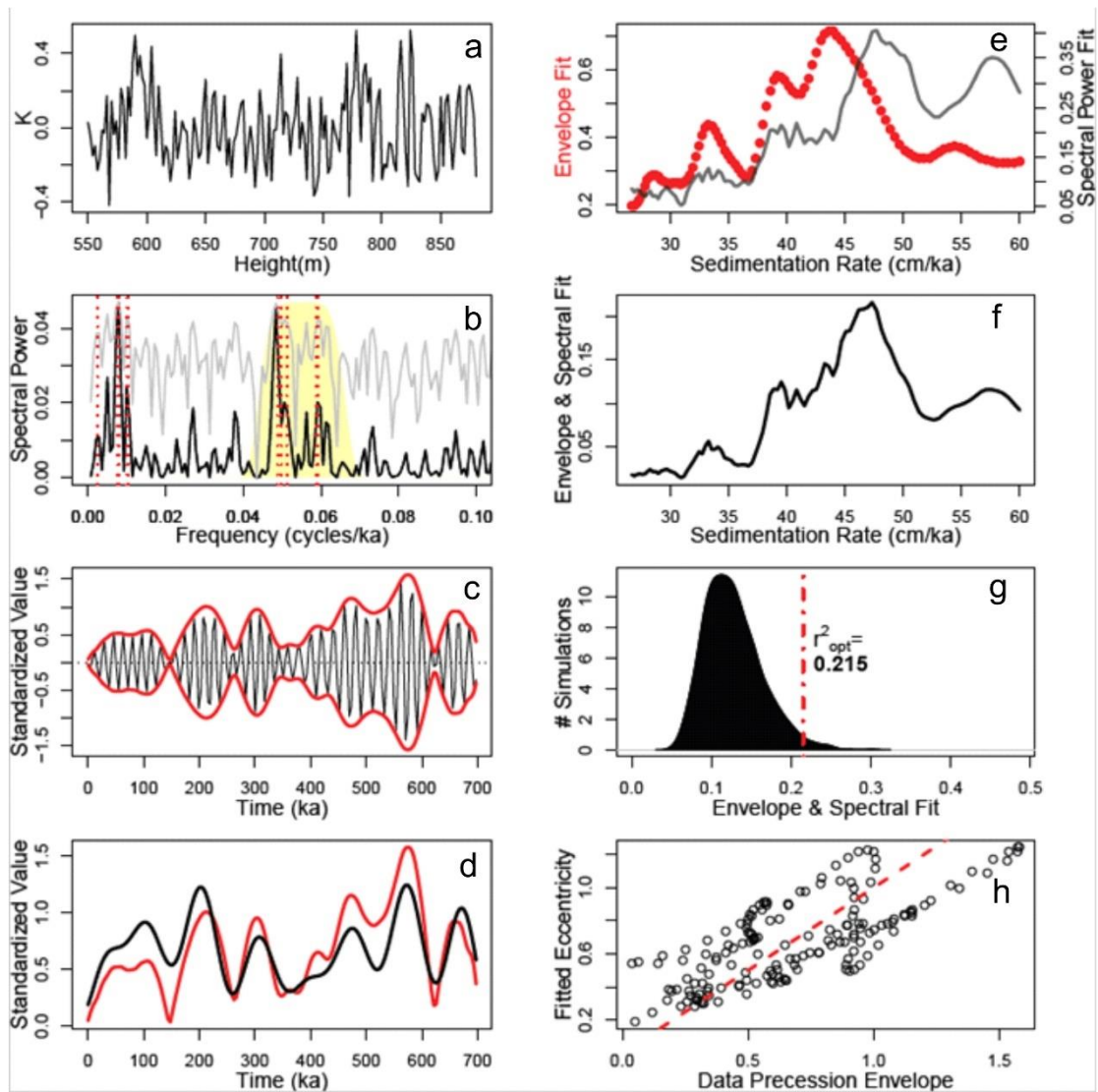
767



768

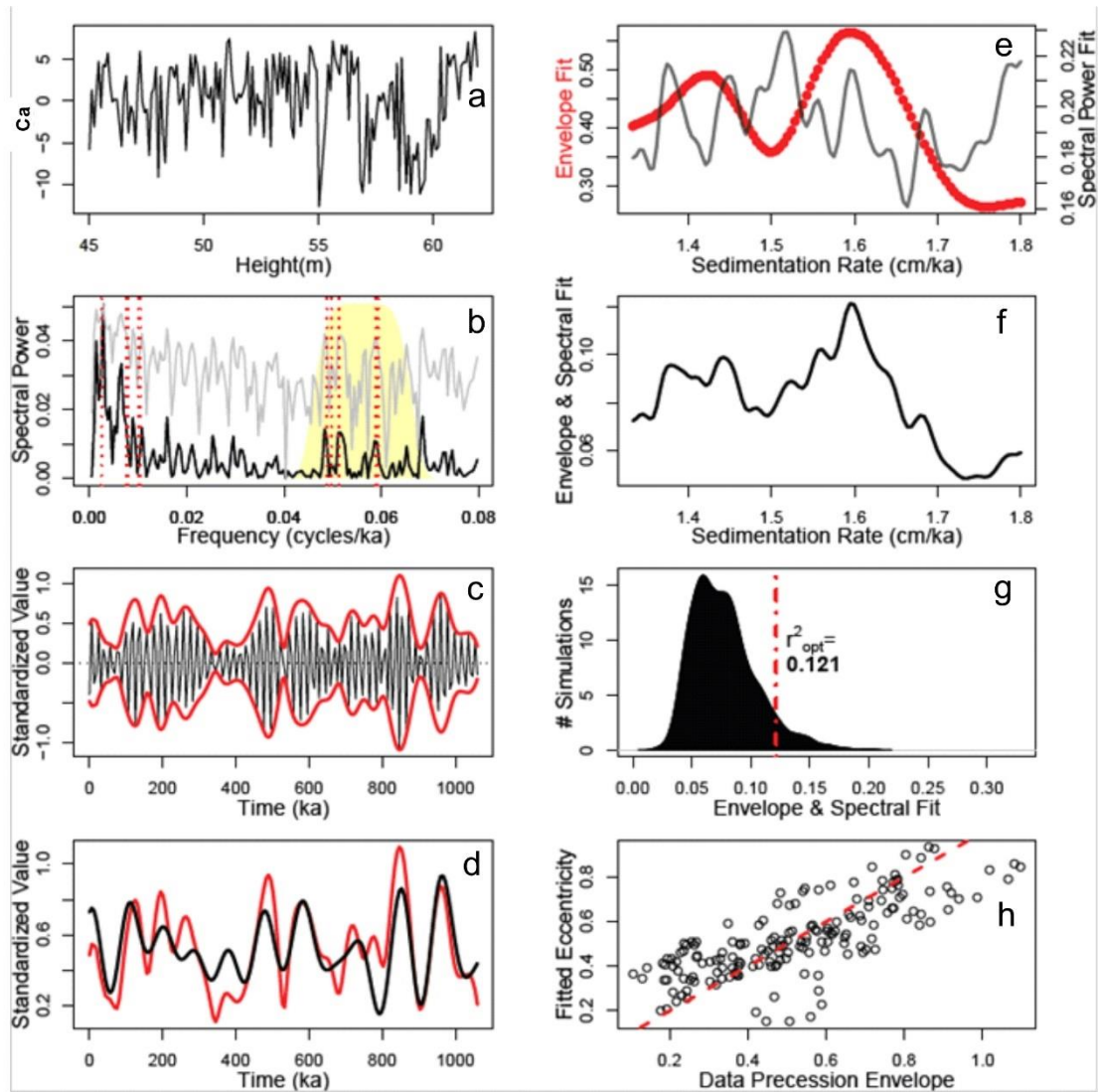
769 **Figure S4.** TimeOpt analysis of the MS series from the Požár-CS section. (a) The MS data of
 770 the Požár-CS section (39). (b) Periodogram for the MS data (black line=linear spectrum; gray
 771 line=log spectrum). Yellow shaded region indicates the portion of the spectrum bandpassed
 772 for evaluation of the precession amplitude envelope. Vertical dashed red line indicate the
 773 eccentricity and climatic precession target periods. (c) Extracting the band-passed precession
 774 signal (black), and the data amplitude envelope (red) determined via Hilbert transform. (d)
 775 Comparison of the data amplitude envelope (red) and the TimeOpt reconstructed eccentricity
 776 model (black). (e) Squared Pearson correlation coefficient for the amplitude envelope fit and
 777 the spectral power fit as a function of sedimentation rate. (f) Combined envelope and spectral
 778 power fit at each evaluated sedimentation rate. (g) Summary of 2000 Monte Carlo simulations
 779 with AR1 surrogates. (h) Cross plot of the data amplitude envelope and the TimeOpt-
 780 reconstructed eccentricity model in panel “d”; dashed red line is the 1:1 line.

781



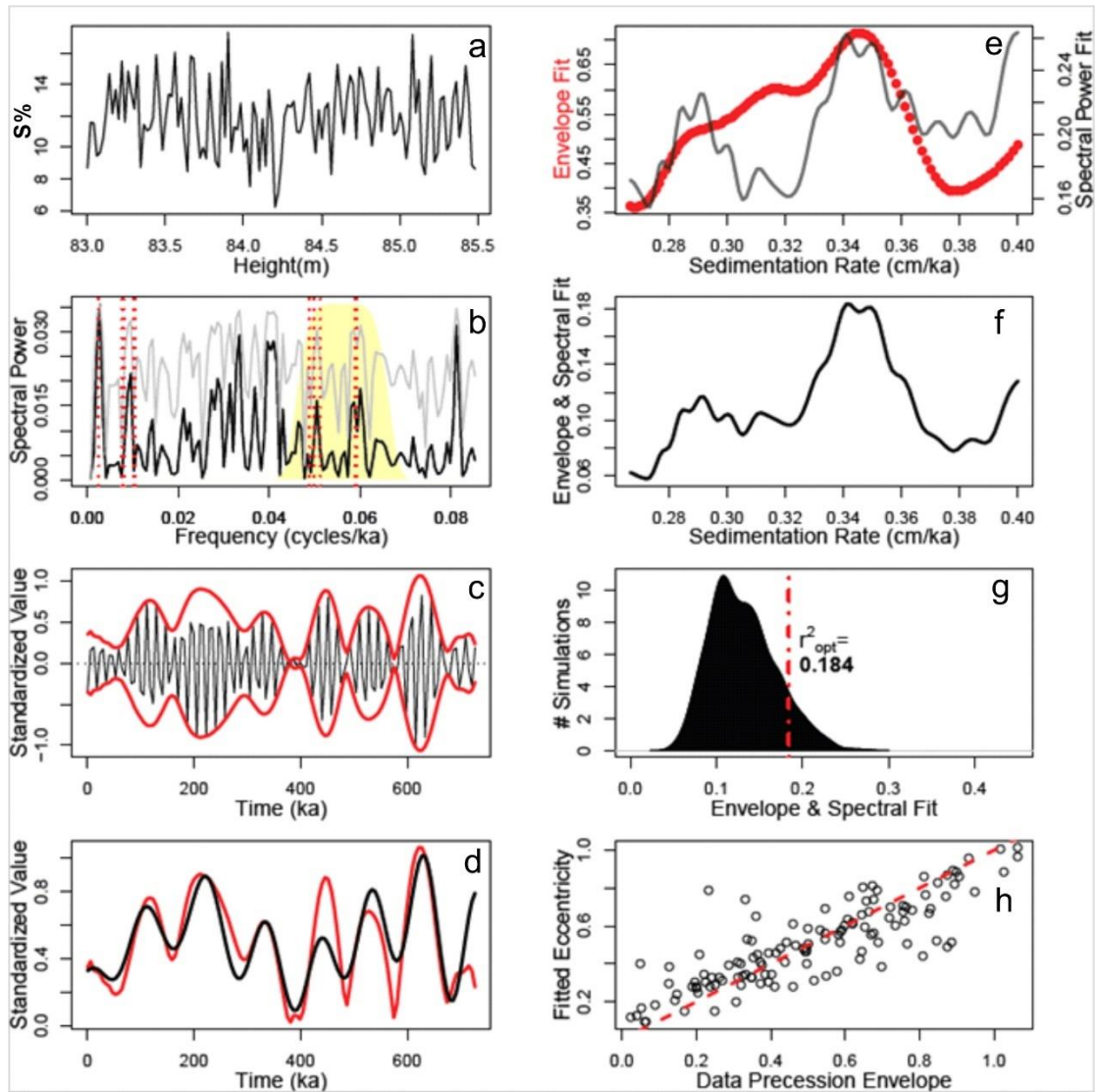
782

783 **Figure S5.** TimeOpt analysis of the K% series from the Upper Ordovician reference section
 784 in Anticosti Island, Canada. (a) The K data of the Upper Ordovician reference section (40).
 785 (b) Periodogram for the K data (black line=linear spectrum; gray line=log spectrum). Yellow
 786 shaded region indicates the portion of the spectrum bandpassed for evaluation of the
 787 precession amplitude envelope. Vertical dashed red line indicate the eccentricity and climatic
 788 precession target periods. (c) Extracting the band-passed precession signal (black), and the
 789 data amplitude envelope (red) determined via Hilbert transform. (d) Comparison of the data
 790 amplitude envelope (red) and the TimeOpt reconstructed eccentricity model (black). (e)
 791 Squared Pearson correlation coefficient for the amplitude envelope fit and the spectral power
 792 fit as a function of sedimentation rate. (f) Combined envelope and spectral power fit at each
 793 evaluated sedimentation rate. (g) Summary of 2000 Monte Carlo simulations with AR1
 794 surrogates. (h) Cross plot of the data amplitude envelope and the TimeOpt-reconstructed
 795 eccentricity model in panel “d”; dashed red line is the 1:1 line.



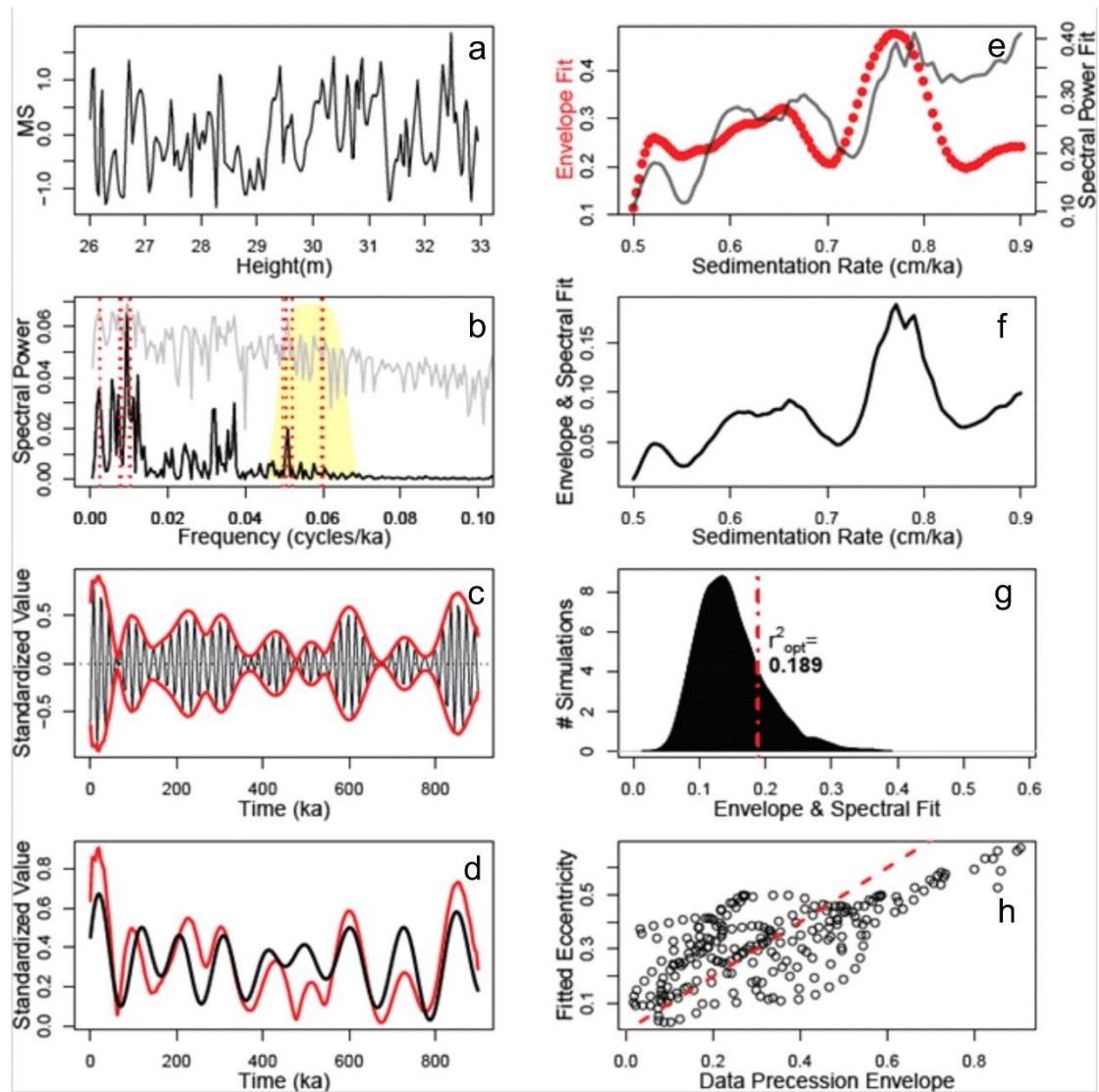
796

797 **Figure S6.** TimeOpt analysis of the Ca% series from the Liangjiashan section. (a) The Ca%
 798 data of the Liangjiashan section (41). (b) Periodogram for the Ca% data (black line=linear
 799 spectrum; gray line=log spectrum). Yellow shaded region indicates the portion of the
 800 spectrum bandpassed for evaluation of the precession amplitude envelope. Vertical dashed
 801 red line indicate the eccentricity and climatic precession target periods. (c) Extracting the
 802 band-passed precession signal (black), and the data amplitude envelope (red) determined via
 803 Hilbert transform. (d) Comparison of the data amplitude envelope (red) and the TimeOpt
 804 reconstructed eccentricity model (black). (e) Squared Pearson correlation coefficient for the
 805 amplitude envelope fit and the spectral power fit as a function of sedimentation rate. (f)
 806 Combined envelope and spectral power fit at each evaluated sedimentation rate. (g) Summary
 807 of 2000 Monte Carlo simulations with AR1 surrogates. (h) Cross plot of the data amplitude
 808 envelope and the TimeOpt-reconstructed eccentricity model in panel “d”; dashed red line is
 809 the 1:1 line.



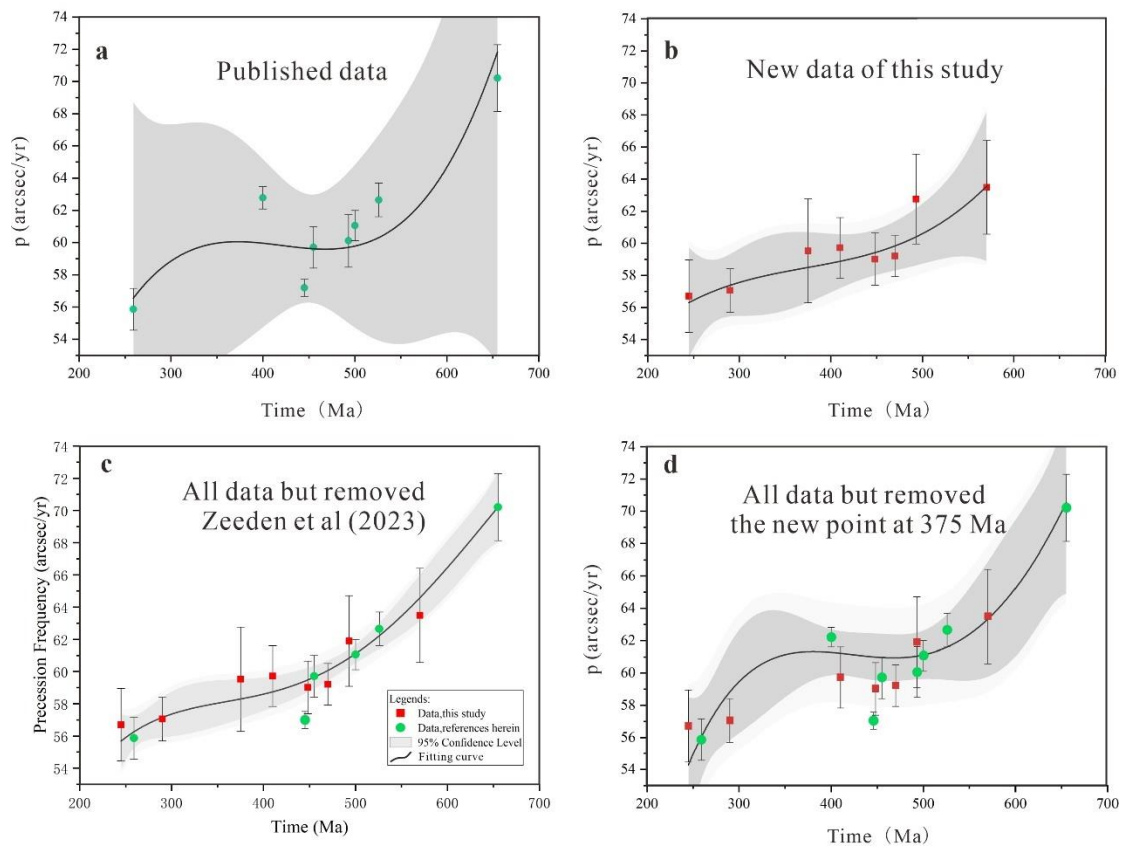
810

811 **Figure S7.** TimeOpt analysis of the S% series from the Alum Shale Formation. (a) The S%
 812 data of the Alum Shale (42). (b) Periodogram for the S% data (black line=linear spectrum;
 813 gray line=log spectrum). Yellow shaded region indicates the portion of the spectrum
 814 bandpassed for evaluation of the precession amplitude envelope. Vertical dashed red line
 815 indicate the eccentricity and climatic precession target periods. (c) Extracting the band-passed
 816 precession signal (black), and the data amplitude envelope (red) determined via Hilbert
 817 transform. (d) Comparison of the data amplitude envelope (red) and the TimeOpt
 818 reconstructed eccentricity model (black). (e) Squared Pearson correlation coefficient for the
 819 amplitude envelope fit and the spectral power fit as a function of sedimentation rate. (f)
 820 Combined envelope and spectral power fit at each evaluated sedimentation rate. (g) Summary
 821 of 2000 Monte Carlo simulations with AR1 surrogates. (h) Cross plot of the data amplitude
 822 envelope and the TimeOpt-reconstructed eccentricity model in panel “d”; dashed red line is
 823 the 1:1 line.



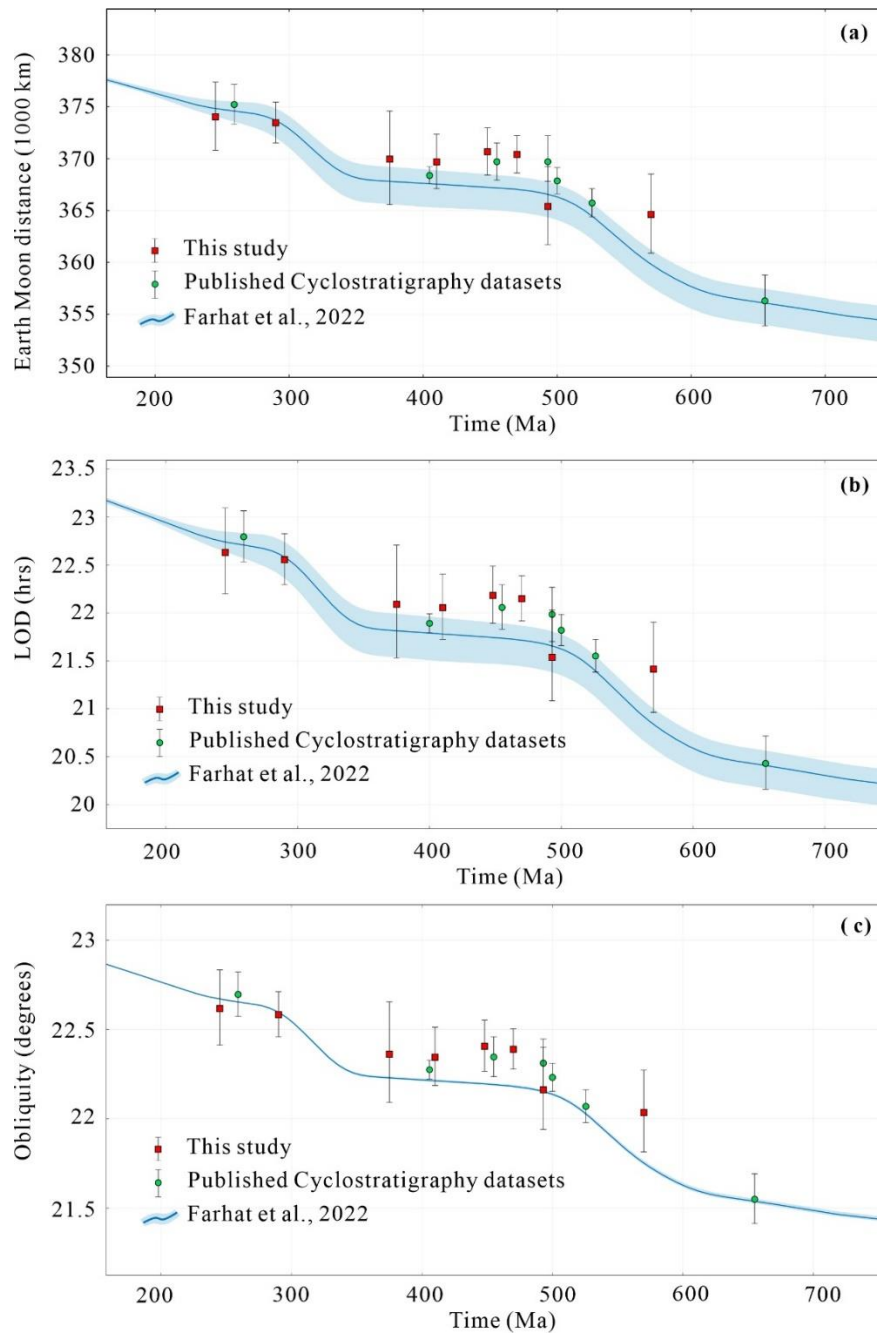
824

825 **Figure S8.** TimeOpt analysis of the MS series from the Doushantuo Formation. (a) The MS
 826 data of the Doushantuo Formation (43). (b) Periodogram for the MS data (black line=linear
 827 spectrum; gray line=log spectrum). Yellow shaded region indicates the portion of the
 828 spectrum bandpassed for evaluation of the precession amplitude envelope. Vertical dashed
 829 red line indicate the eccentricity and climatic precession target periods. (c) Extracting the
 830 band-passed precession signal (black), and the data amplitude envelope (red) determined via
 831 Hilbert transform. (d) Comparison of the data amplitude envelope (red) and the TimeOpt
 832 reconstructed eccentricity model (black). (e) Squared Pearson correlation coefficient for the
 833 amplitude envelope fit and the spectral power fit as a function of sedimentation rate. (f)
 834 Combined envelope and spectral power fit at each evaluated sedimentation rate. (g) Summary
 835 of 2000 Monte Carlo simulations with AR1 surrogates. (h) Cross plot of the data amplitude
 836 envelope and the TimeOpt-reconstructed eccentricity model in panel “d”; dashed red line is
 837 the 1:1 line.



838

839 **Figure S9.** Fitting the reconstructed precession frequencies from 200 Ma to 700 Ma. (a) The
 840 fitting curve of the published data is derived from the cubic polynomial fitting. Evidently,
 841 there are a wide range of possibility of the fitting result. (b) The new data is also used the
 842 cubic polynomial fitting to find out their trends and variations. (c) Fitting all of the data but
 843 except the data from Zeeden et al. (2023). (d) After removing the data point at 375 Ma, we
 844 have fitted the rest of data by using the quartic polynomial fitting approach, the fitting curve
 845 has shown a clearly staircase pattern.

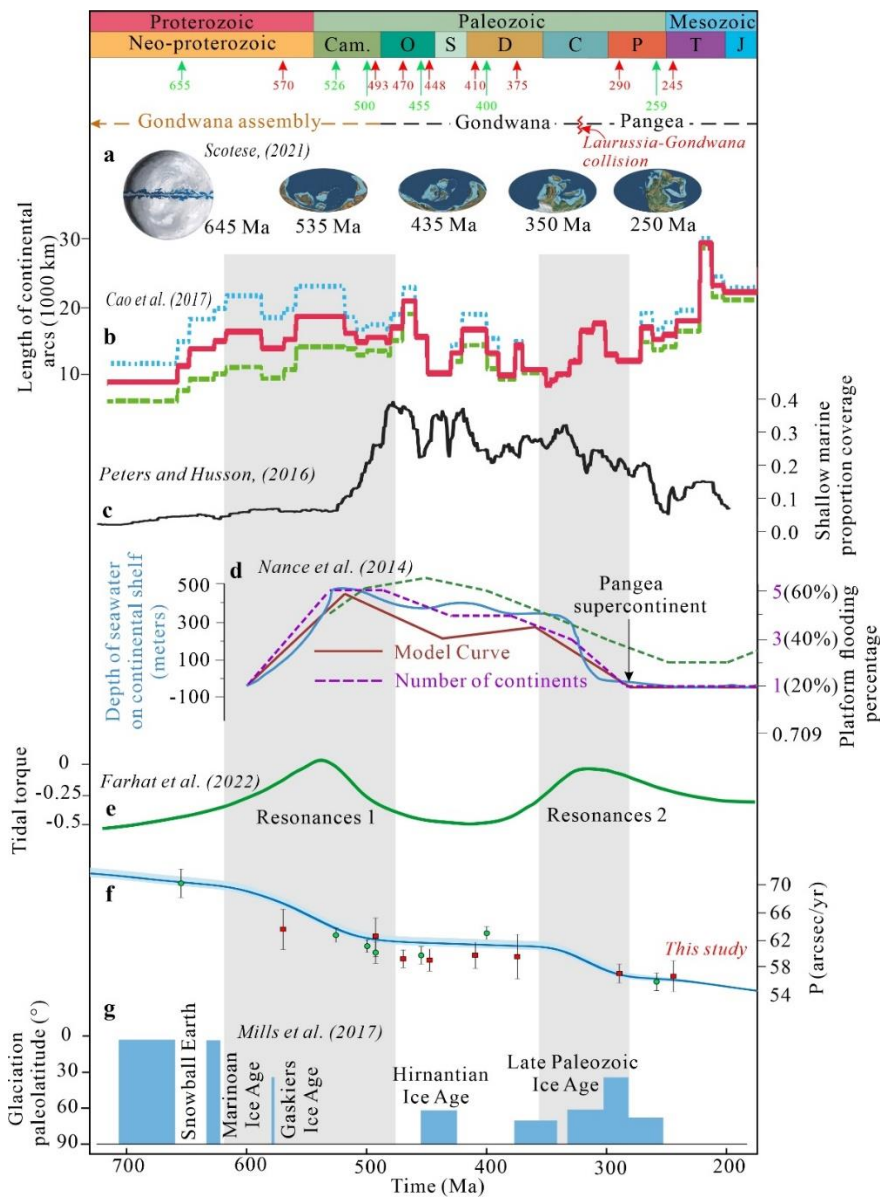


846

847 **Figure S10.** Reconstruction of the (a) Earth-Moon distance (EMD), (b) length of solar day
 848 (LOD) and (c) obliquity degrees based on the Earth's precession frequency (p) results
 849 originated from the TimeOptMCMC analysis. The red square dots are calculated from this
 850 study, while the green circle dots are compiled from the published research articles (reference
 851 herein). The EMD, LOD and obliquity degrees were obtained from the *AstroGeo22* tool on
 852 the *AsotroGeo* website (<http://www.astrogeo.eu/>).

853

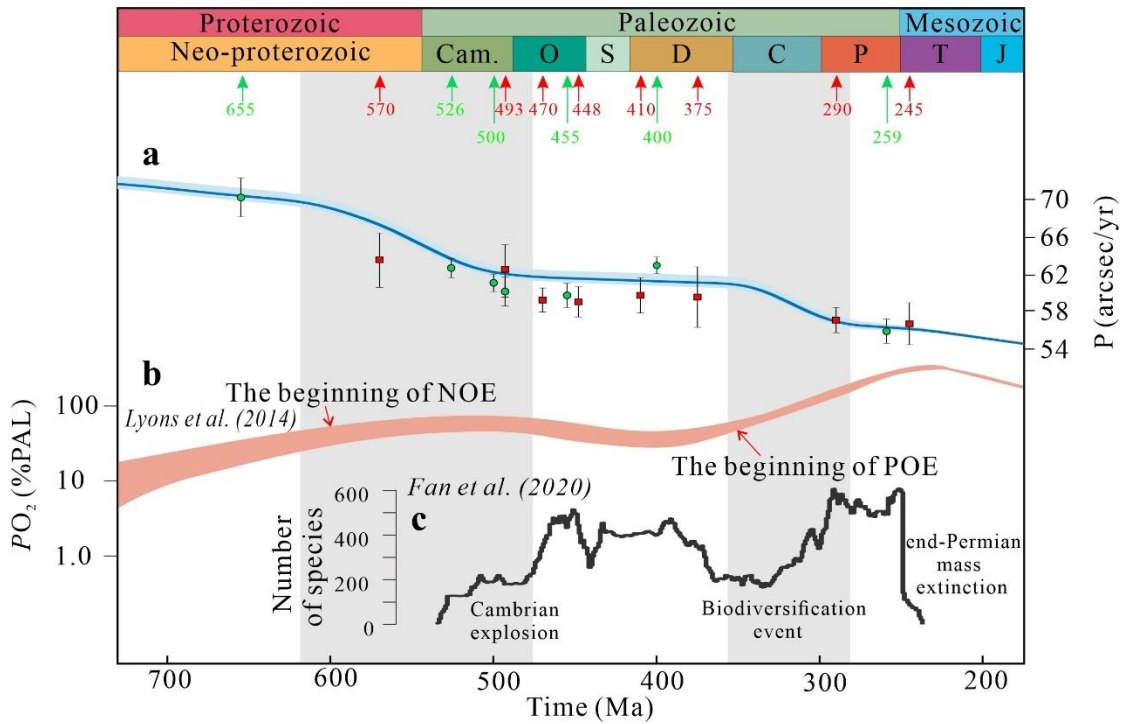
854



855

856 **Figure. S11.** Correlation between the Earth's rotation rate and the trends of multiple tectonic
 857 and environmental records. (a). The paleogeographic maps of Earth (62). (b). Continental arc
 858 length in the past 750 Ma (49). Dotted blue, dashed green, and solid red curves are the
 859 maximum, minimum, and average length estimates, respectively. (c). The shallow marine
 860 proportion coverage curve (50). (d). The depth of seawater on continental shelf, the degree of
 861 platform flooding and the number of continents from the past ~600 Ma to ~190 Ma (51). (e).
 862 The simulated tidal torque and normalized its absolute strength to present value (16). (f). The
 863 estimated Earth's precession frequency from geological archives, the blue curve represents
 864 the F22 tidal model (16). (g). Paleolatitude of glaciations throughout the Neoproterozoic to
 865 Paleozoic (63).

866



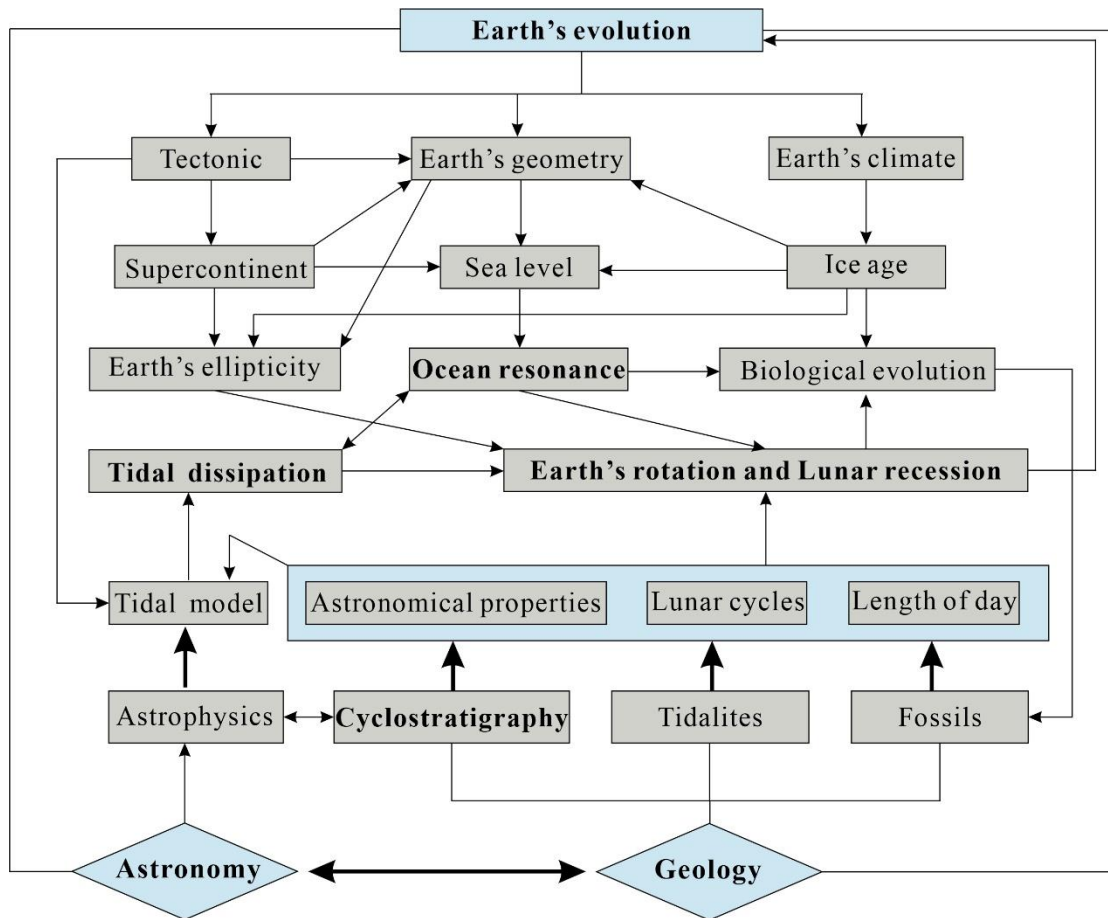
867

868 **Figure. S12.** Correlation between the Earth's rotation rate and the trends of oxygen
 869 concentration and species abundance curves. (a). The estimated Earth's precession frequency
 870 from geological archives, the blue curve represents the F22 tidal model (16). (b). The
 871 evolution of Earth's atmospheric oxygen content from Neoproterozoic to Mesozoic Eras (58).
 872 (c). The species diversity from Cambrian to Triassic (59).

873

874

875



876

877 **Figure S13.** The possible cause-and-effect between the Earth's rotational dynamics and
878 geological processes. In this framework, the variations of the Earth-Moon tidal dissipation
879 and Earth dynamic ellipticity dynamic are two main factors that influence Earth's rotation
880 deceleration. Understanding these connections requires interdisciplinary research combining
881 astrophysics, geophysics, geology, climatology, and other relevant fields. Additionally,
882 international collaborations are necessary to solve these complex issues (e.g., *AstroGeo*
883 project in the Europe and *CycloAstro* project in the U. S).

884

885

886

887 **Supplementary R scripts**

888

889 The R Scripts for TimeOpt and TimeOptMCMC analysis for this paper

890

891 **##Conduct the TimeOpt and TimtOptMCMC analysis to obtain the precessional constant**
892 **index (p)**

893 **### GR data from Li et al (2018 EPSL), GR series 10-72 m (245 Ma)**

894 library(astrochron)

895 data=read();

896 data1=iso(data,xmin=10,xmax=72);

897 data1=trim(data1,c=2);

898 data1=noKernel(data1,smooth=0.1);

899 **### Interpolate the data to the median sampling interval**

900 data1=linterp(data1)

901 **###Determine nominal precession and eccentricity periods,then conduct nominal timeOpt**
902 **analysis**

903 targetTot=calcPeriods(g=c(5.525000,7.455000,17.300000,17.850000,4.257455),k=54.5,output
904 t=2);

905 targetE=sort(targetTot[1:5],decreasing=T);

906 targetP=sort(targetTot[6:10],decreasing=T);

907 **###run nominal timeOpt and output sedimentation rate grid and fit**

908 res1=timeOpt(data1,sedmin=4,sedmax=7,numsed=100,targetE=targetE,targetP=targetP,flow=
909 1/23,fhigh=1/17,roll=10^7,limit=T,output=1);

910 **###output optimal time series, bandpassed series, amplitude envelope and TimeOpt-**
911 **reconstructed eccentricity**

912 res2=timeOpt(data1,sedmin=4,sedmax=7,numsed=100,targetE=targetE,targetP=targetP,flow=
913 1/23,fhigh=1/17,roll=10^7,limit=T,output=2);

```

914 ###perform nominal timeOpt significance testing
915 simres=timeOptSim(data1,sedmin=4,sedmax=7,numsed=100,targetE=targetE,targetP=targetP
916 ,flow=1/23,fhigh=1/17,roll=10^7,numsim=1000,output=2,ncores=4);
917 ###plot summary figure
918 timeOptPlot(data1,res1,res2,simres,flow=1/23,fhigh=1/17,fitR=0.20783,roll=10^7,targetE=ta
919 rgetE,targetP=targetP,xlab="Height(cm)",ylab="GR",verbose=T);
920 ###run a single timeOptMCMC chain (100 chains)
921 res=timeOptMCMC(data1,sedmin=4,sedmax=7,sedstart=5.94,gAve=c(5.525000,7.455000,17
922 .300000,17.850000,4.257455), gSd=c(0.12500,0.01500,0.150005,0.15000,0.00002),gstart=c(-
923 1,-1,-1,-1,-1),kAve=54.5,kSd=2.5,kstart=-
924 1,rhomin=0,rhomin=0.9999,rhomin=1,sigmamin=NULL,sigmamax=NULL,sigmastart=-
925 1,nsamples=200000,
926 iopt=1,epsilon=c(0.2,0.2,0.35,0.35,0.8,0.85,0.6,0.35,0.9,0.35,0.9)/40,ran=T,burnin=-
927 1,savefile = F);
928 ### output the TimeOptMCMC results
929 write.table(res,file="Li_GR_TimeOptMCMC_results.csv",sep=" ",row.names=FALSE)
930
931
932 ###TimeOptMCMC analysis the Ji251 NGR series from Huang et al., 2020_P3 (290Ma)
933 library(astrochron);
934 ###Obtain the target dataset
935 ji=read()
936 ji251=iso(ji,xmin=3650,xmax=3770);
937 ji1=trim(ji251,c=3);
938 ji2=linterp(ji1,dt=0.5);
939 ###Determine nominal precession and eccentricity periods,then conduct nominal timeOpt
940 analysis
941 targetTot=calcPeriods(g=c(5.525000,7.455000,17.300000,17.850000,4.257455),k=55,output
942 =2);
943 targetE=sort(targetTot[1:5],decreasing=T);

```

```

944 targetP=sort(targetTot[6:10],decreasing=T);
945 ###run nominal timeOpt and output sedimentation rate grid and fit
946 res1=timeOpt(ji2,sedmin=2,sedmax=18,numsed=100,targetE=targetE,targetP=targetP,flow=1
947 /23,fhigh=1/16,roll=10^7,limit=T,output=1);
948 ###output optimal time series, bandpassed series, amplitude envelope and TimeOpt-
949 reconstructed eccentricity
950 res2=timeOpt(ji2,sedmin=2,sedmax=18,numsed=100,targetE=targetE,targetP=targetP,flow=1
951 /23,fhigh=1/16,roll=10^7,limit=T,output=2);
952 ###perform nominal timeOpt significance testing
953 simres=timeOptSim(ji2,sedmin=2,sedmax=18,numsed=100,targetE=targetE,targetP=targetP,f
954 low=1/23,fhigh=1/16,roll=10^7,numsim=2000,output=2,ncores=6);
955 ###plot summary figure
956 timeOptPlot(ji2,res1,res2,simres,flow=1/23,fhigh=1/16,fitR=0.19915,roll=10^7,targetE=targe
957 tE,targetP=targetP,xlab="Height(m)",ylab="NGR",verbose=T);
958 ###run a single timeOptMCMC chain (150 chain)
959 res=timeOptMCMC(ji2,sedmin=2,sedmax=18,sedstart=9.78,gAve=c(5.525000,7.455000,17.3
960 00000,17.850000,4.257455),gSd=c(0.12500,0.01500,0.150005,0.15000,0.00002),gstart=c(-
961 1,-1,-1,-1,-1),kAve=55,kSd=3,kstart=-1,rhomin=0,rhomin=0.9999,rhostart=-
962 1,sigmamin=NULL,sigmax=NULL,sigmastart=1,nsamples=100000,iopt=1,epsilon=c(0.2,
963 0.2,0.35,0.35,0.8,0.85,0.6,0.35,0.9,0.35,0.9)/20,ran=T,burnin=-1);
964 ### output the TimeOptMCMC results
965 write.table(res,file="Huang_NGR_TimeOptMCMC_results.csv",sep="," ,row.names=FALSE)
966
967
968 ### Data from De Vleeschouwer et al (2017 Nature Communications) H32_MS series, 176-
969 900cm (~375 Ma)
970 ###(1)load the Astrochron package
971 library(astrochron);
972 ###(2) Obtain the target dataset
973 data=read();

```

```

974 data1=iso(data,xmin=176,xmax=900);
975 # Convert depth from cm to m
976 data1[1]=data1[1]/100
977 data1=noKernel(data1,smooth=0.1);
978 data1=trim(data1,c=1.5);
979 ###(3) Interpolate the data to the median sampling interval
980 data1=linterp(data1);
981 ###Determine nominal precession and eccentricity periods,then conduct nominal timeOpt
982 analysis
983 targetTot=calcPeriods(g=c(5.525000,7.455000,17.300000,17.850000,4.257455),k=58,output
984 =2);
985 targetE=sort(targetTot[1:5],decreasing=T);
986 targetP=sort(targetTot[6:10],decreasing=T);
987 ###run nominal timeOpt and output sedimentation rate grid and fit
988 res1=timeOpt(data1,sedmin=0.7,sedmax=1,numsed=100,targetE=targetE,targetP=targetP,flow
989 w=1/23,fhigh=1/16,roll=10^7,limit=T,output=1);
990 ###output optimal time series, bandpassed series, amplitude envelope and TimeOpt-
991 reconstructed eccentricity
992 res2=timeOpt(data1,sedmin=0.7,sedmax=1,numsed=100,targetE=targetE,targetP=targetP,flow
993 w=1/23,fhigh=1/16,roll=10^7,limit=T,output=2);
994 ###perform nominal timeOpt significance testing
995 simres=timeOptSim(data1,sedmin=0.7,sedmax=1,numsed=100,targetE=targetE,targetP=target
996 tP,flow=1/23,fhigh=1/16,roll=10^7,numsim=2000,output=2,ncores=6);
997 ###plot summary figure
998 timeOptPlot(data1,res1,res2,simres,flow=1/23,fhigh=1/16,fitR=0.18966,roll=10^7,targetE=targetE,
999 targetP=targetP,xlab="Height(m)",ylab="MS",verbose=T);
1000 ###run a single timeOptMCMC chain (200 chain)
1001 res=timeOptMCMC(data1,sedmin=0.7,sedmax=1,sedstart=0.83,gAve=c(5.525000,7.455000,
1002 17.300000,17.850000,4.257455),gSd=c(0.12500,0.01500,0.150005,0.15000,0.00002),gstart=

```

```

1003 c(-1,-1,-1,-1,-1),kAve=58,kSd=4,kstart=-1,rhomin=0,rhobox=0.9999,rhostart=-
1004 1,sigmamin=NULL,sigmax=NULL,sigmastart=-1,nsamples=100000,
1005 iopt=1,epsilon=c(0.2,0.2,0.35,0.35,0.8,0.85,0.6,0.35,0.9,0.35,0.9)/20,ran=T,burnin=-1);
1006 ### output the TimeOptMCMC results
1007 write.table(res,file="David_MS_375Ma_TimeOptMCMC_results.csv",sep="," ,row.names=F
1008 ALSE)
1009
1010 ### Data from Da Silva et al (2016 EPSL) Požár-CS section_MS series (106.7-114m), (~410
1011 Ma).
1012 ###(1)load the Astrochron package
1013 library(astrochron);
1014 ###(2) Obtain the target dataset
1015 data=read();
1016 data1=iso(data,xmin=106.7,xmax=114);
1017 data1=noKernel(data1,smooth=0.5);
1018 data1=trim(data1,c=2);
1019 ###(3) Interpolate the data to the median sampling interval
1020 data1=linterp(data1);
1021 ###Determine nominal precession and eccentricity periods,then conduct nominal timeOpt
1022 analysis
1023 targetTot=calcPeriods(g=c(5.525000,7.455000,17.300000,17.850000,4.257455),k=58,output
1024 =2);
1025 targetE=sort(targetTot[1:5],decreasing=T);
1026 targetP=sort(targetTot[6:10],decreasing=T);
1027 ###run nominal timeOpt and output sedimentation rate grid and fit
1028 res1=timeOpt(data1,sedmin=0.2,sedmax=1,numsed=100,targetE=targetE,targetP=targetP,flo
1029 w=1/25,fhigh=1/16,roll=10^7,limit=T,output=1);

```

```

1030 ###output optimal time series, bandpassed series, amplitude envelope and TimeOpt-
1031 reconstructed eccentricity

1032 res2=timeOpt(data1,sedmin=0.2,sedmax=1,numsed=100,targetE=targetE,targetP=targetP,flo
1033 w=1/25,fhigh=1/16,roll=10^7,limit=T,output=2);

1034 ###perform nominal timeOpt significance testing

1035 simres=timeOptSim(data1,sedmin=0.2,sedmax=1,numsed=100,targetE=targetE,targetP=targe
1036 tP,flow=1/25,fhigh=1/16,roll=10^7,numsim=2000,output=2,ncores=6);

1037 ###plot summary figure

1038 timeOptPlot(data1,res1,res2,simres,flow=1/25,fhigh=1/16,fitR=0.162,roll=10^7,targetE=targe
1039 tE,targetP=targetP,xlab="Height(m)",ylab="MS",verbose=T);

1040 ###run a single timeOptMCMC chain (150 chain)

1041 res=timeOptMCMC(data1,sedmin=0.2,sedmax=1,sedstart=0.83,gAve=c(5.525000,7.455000,
1042 17.300000,17.850000,4.257455),gSd=c(0.12500,0.01500,0.150005,0.15000,0.00002),gstart=
1043 c(-1,-1,-1,-1,-1),kAve=58,kSd=4,kstart=-1,rhomin=0,rhomin=0,rhomin=0.9999,rhomin=-
1044 1,sigmamin=NULL,sigmamax=NULL,sigmastart=-1,nsamples=200000,

1045 iopt=1,epsilon=c(0.2,0.2,0.35,0.35,0.8,0.85,0.6,0.35,0.9,0.35,0.9)/20,ran=T,burnin=-1);

1046 ### output the TimeOptMCMC results

1047 write.table(res,file="Dasilva_MS_410Ma_TimeOptMCMC_results.csv",sep=" ",row.names=
1048 FALSE)

1049

1050 ### Data from Sinnesael et al (2021 Geology) 550-900 m K% time series (~448 Ma)

1051 ###(2) Obtain the target dataset

1052 library(astrochron);

1053 data=read()

1054 data1=noKernel(data,smooth=0.1);

1055 data1=iso(data1,xmin=550,xmax=900);

1056 data1=trim(data1,c=1.5);

1057 data2=linterp(data1,dt=2);

```

```

1058 ###Determine nominal precession and eccentricity periods,then conduct nominal timeOpt
1059 analysis

1060 targetTot=calcPeriods(g=c(5.525000,7.455000,17.300000,17.850000,4.257455),k=59,output
1061 =2);

1062 targetE=sort(targetTot[1:5],decreasing=T);

1063 targetP=sort(targetTot[6:10],decreasing=T);

1064 ###run nominal timeOpt and output sedimentation rate grid and fit

1065 res1=timeOpt(data2,sedmin=10,sedmax=60,numsed=100,targetE=targetE,targetP=targetP,flow=1/23,fhigh=1/15,roll=10^7,limit=T,output=1);
1066

1067 ###output optimal time series, bandpassed series, amplitude envelope and TimeOpt-
1068 reconstructed eccentricity

1069 res2=timeOpt(data2,sedmin=10,sedmax=60,numsed=100,targetE=targetE,targetP=targetP,flow=1/23,fhigh=1/15,roll=10^7,limit=T,output=2);
1070

1071 ###perform nominal timeOpt significance testing

1072 simres=timeOptSim(data2,sedmin=10,sedmax=60,numsed=100,targetE=targetE,targetP=targetP,flow=1/23,fhigh=1/15,roll=10^7,numsim=2000,output=2,ncores=6);
1073

1074 ###plot summary figure

1075 timeOptPlot(data2,res1,res2,simres,flow=1/23,fhigh=1/15,fitR=0.21654,roll=10^7,targetE=targetE,targetP=targetP,xlab="Height(m)",ylab="K",verbose=T);
1076

1077 ###run a single timeOptMCMC chain (100 chain)

1078 res=timeOptMCMC(data2,sedmin=10,sedmax=60,sedstart=47.3,gAve=c(5.525000,7.455000,
1079 17.300000,17.850000,4.257455),gSd=c(0.12500,0.01500,0.150005,0.15000,0.00002),gstart=
1080 c(-1,-1,-1,-1,-1),kAve=59,kSd=4,kstart=-1,rhomin=0,rhomin=0,rhomin=0.9999,rhomin=0.9999,rhomin=0.9999,rhomin=0.9999,
1081 1,sigmamin=NULL,sigmax=NULL,sigstart=1,nsamples=200000,

1082 iopt=1,epsilon=c(0.2,0.2,0.35,0.35,0.8,0.85,0.6,0.35,0.9,0.35,0.9)/20,ran=T,burnin=-1);

1083 ### output the TimeOptMCMC results

1084 write.table(res,file="Sinnesael_K_445Ma_TimeOptMCMC_results.csv",sep="," ,row.names=
1085 FALSE)

1086

1087 ### Data from Ma et al (2019 P3) LJS Ca% time series (~470 Ma)

```



```

1088
1089 ###(2) Obtain the target dataset
1090 library(astrochron);
1091 data=read()
1092 data1=iso(data,xmin=45,xmax=62)
1093 data1=noKernel(data1,smooth=0.5);
1094 data1=trim(data1,c=1.5);
1095 data2=linterp(data1,dt=0.1);
1096 ###Determine nominal precession and eccentricity periods,then conduct nominal timeOpt
1097 analysis
1098 targetTot=calcPeriods(g=c(5.525000,7.455000,17.300000,17.850000,4.257455),k=59,output
1099 =2);
1100 targetE=sort(targetTot[1:5],decreasing=T);
1101 targetP=sort(targetTot[6:10],decreasing=T);
1102 ###run nominal timeOpt and output sedimentation rate grid and fit
1103 res1=timeOpt(data2,sedmin=0.1,sedmax=1.8,numsed=100,targetE=targetE,targetP=targetP,fl
1104 ow=1/22,fhigh=1/15,roll=10^7,limit=T,output=1);
1105 ###output optimal time series, bandpassed series, amplitude envelope and TimeOpt-
1106 reconstructed eccentricity
1107 res2=timeOpt(data2,sedmin=0.1,sedmax=1.8,numsed=100,targetE=targetE,targetP=targetP,fl
1108 ow=1/22,fhigh=1/15,roll=10^7,limit=T,output=2);
1109 ###perform nominal timeOpt significance testing
1110 simres=timeOptSim(data2,sedmin=0.1,sedmax=1.8,numsed=100,targetE=targetE,targetP=tar
1111 getP,flow=1/22,fhigh=1/15,roll=10^7,numsim=2000,output=2,ncores=6);
1112 ###plot summary figure
1113 timeOptPlot(data2,res1,res2,simres,flow=1/22,fhigh=1/15,fitR=0.12135,roll=10^7,targetE=ta
1114 rgetE,targetP=targetP,xlab="Height(m)",ylab="Ca",verbose=T);
1115 ###run a single timeOptMCMC chain (50 chain)

```

```

1116 res=timeOptMCMC(data2,sedmin=0.1,sedmax=1.8,sedstart=1.59,gAve=c(5.525000,7.45500
1117 0,17.300000,17.850000,4.257455),gSd=c(0.12500,0.01500,0.150005,0.15000,0.00002),gstart
1118 =c(-1,-1,-1,-1,-1),kAve=59,kSd=5,kstart=-1,rhomin=0,rhobox=0.9999,rhostart=-
1119 1,sigmamin=NULL,sigmax=NULL,sigmastart=1,nsamples=600000,

1120 iopt=1,epsilon=c(0.2,0.2,0.35,0.35,0.8,0.85,0.6,0.35,0.9,0.35,0.9)/40,ran=T,burnin=-1);

1121 ### output the TimeOptMCMC results

1122 write.table(res,file="Ma_Ca_470Ma_TimeOptMCMC_results.csv",sep="," ,row.names=FALS
1123 E)

1124

1125 ##### Data from Sorensen et al (2020 EPSL) S% (83-85.5m) time series (~493 Ma)

1126 library(astrochron);

1127 ###Obtain the target dataset

1128 Soren=read();

1129 ###Interpolate the data to the median sampling interval

1130 Soren1=linterp(Soren,dt=0.01);

1131 Soren2=iso(Soren1,xmin=83, xmax=85.5);

1132 Soren2=trim(Soren2,c=1.5);

1133 Soren2=linterp(Soren2,dt=0.02);

1134 ###Determine nominal precession and eccentricity periods,then conduct nominal timeOpt
1135 analysis

1136 targetTot=calcPeriods(g=c(5.525000,7.455000,17.300000,17.850000,4.257455),k=59,output
1137 =2);

1138 targetE=sort(targetTot[1:5],decreasing=T);

1139 targetP=sort(targetTot[6:10],decreasing=T);

1140 ###run nominal timeOpt and output sedimentation rate grid and fit

1141 res1=timeOpt(Soren2,sedmin=0.1,sedmax=0.4,numsed=100,targetE=targetE,targetP=targetP,
1142 flow=1/22,fhigh=1/15,roll=10^7,limit=T,output=1);

1143 ###output optimal time series, bandpassed series, amplitude envelope and TimeOpt-
1144 reconstructed eccentricity

```

```

1145 res2=timeOpt(Soren2,sedmin=0.1,sedmax=0.4,numsed=100,targetE=targetE,targetP=targetP,
1146 flow=1/22,fhigh=1/15,roll=10^7,limit=T,output=2);

1147 ###perform nominal timeOpt significance testing

1148 simres=timeOptSim(Soren2,sedmin=0.1,sedmax=0.4,numsed=100,targetE=targetE,targetP=ta
1149 rgetP,flow=1/22,fhigh=1/15,roll=10^7,numsim=2000,output=2,ncores=6);

1150 ###plot summary figure

1151 timeOptPlot(Soren2,res1,res2,simres,flow=1/22,fhigh=1/15,fitR=0.18408,roll=10^7,targetE=t
1152 argetE,targetP=targetP,xlab="Height(m)",ylab="S",verbose=T);

1153 ###run a single timeOptMCMC chain (100 chain)

1154 res=timeOptMCMC(Soren2,sedmin=0.1,sedmax=0.5,sedstart=0.34,gAve=c(5.525000,7.4550
1155 00,17.300000,17.850000,4.257455),gSd=c(0.12500,0.01500,0.150005,0.15000,0.00002),gsta
1156 rt=c(-1,-1,-1,-1,-1),kAve=59,kSd=5,kstart=-1,rhomin=0,rhomin=0,rhomin=0.9999,rhostart=-
1157 1,sigmamin=NULL,sigmamax=NULL,sigmastart=1,nsamples=200000,

1158 iopt=1,epsilon=c(0.2,0.2,0.35,0.35,0.8,0.85,0.6,0.35,0.9,0.35,0.9)/40,ran=T,burnin=-1);

1159 ### output the TimeOptMCMC results

1160 write.table(res,file="Sorensen_S%_493Ma_TimeOptMCMC_results.csv",sep="," ,row.names
1161 =FALSE)

1162

1163 ### Data from Li et al (2022, Global and Planetary Changes) MS time series (570 Ma)

1164 library(astrochron);

1165 ###Obtain the target dataset

1166 Li=read();

1167 ### Interpolate the data to the median sampling interval

1168 Li=linterp(Li);

1169 Li_1=iso(Li,xmin=26,xmax=33);

1170 Li_2=noKernel(Li_1,smooth=0.5);

1171 Li_3=trim(Li_2,c=1.5);

1172 Li_4=linterp(Li_3,dt=0.03);

```

```

1173 ###Determine nominal precession and eccentricity periods,then conduct nominal timeOpt
1174 analysis

1175 targetTot=calcPeriods(g=c(5.525000,7.455000,17.300000,17.850000,4.257455),k=60,output
1176 =2);

1177 targetE=sort(targetTot[1:5],decreasing=T);

1178 targetP=sort(targetTot[6:10],decreasing=T);

1179 ###run nominal timeOpt and output sedimentation rate grid and fit

1180 res1=timeOpt(Li_4,sedmin=0.5,sedmax=0.9,numsed=100,targetE=targetE,targetP=targetP,flow=1/21,fhigh=1/15,roll=10^7,limit=T,output=1);
1181

1182 ###output optimal time series, bandpassed series, amplitude envelope and TimeOpt-
1183 reconstructed eccentricity

1184 res2=timeOpt(Li_4,sedmin=0.5,sedmax=0.9,numsed=100,targetE=targetE,targetP=targetP,flow=1/21,fhigh=1/15,roll=10^7,limit=T,output=2);
1185

1186 ###perform nominal timeOpt significance testing

1187 simres=timeOptSim(Li_4,sedmin=0.5,sedmax=0.9,numsed=100,targetE=targetE,targetP=targetP,flow=1/21,fhigh=1/15,roll=10^7,numsim=2000,output=2,ncores=6);
1188

1189 ###plot summary figure

1190 timeOptPlot(Li_4,res1,res2,simres,flow=1/21,fhigh=1/15,fitR=0.1889,roll=10^7,targetE=targetE,targetP=targetP,xlab="Height(m)",ylab="MS",verbose=T);
1191

1192 ###run a single timeOptMCMC chain (100 chain)

1193 res=timeOptMCMC(Li_4,sedmin=0.5,sedmax=0.9,sedstart=0.77,gAve=c(5.525000,7.455000
1194 ,17.300000,17.850000,4.257455),gSd=c(0.12500,0.01500,0.150005,0.15000,0.00002),gstart=
1195 c(-1,-1,-1,-1,-1),kAve=60,kSd=5,kstart=-1,rhomin=0,rhomin=0.9999,rhostart=-
1196 1,sigmamin=NULL,sigmax=NULL,sigmastart=1,nsamples=200000,

1197 iopt=1,epsilon=c(0.2,0.2,0.35,0.35,0.8,0.85,0.6,0.35,0.9,0.35,0.9)/20,ran=T,burnin=-1);

1198 ### output the TimeOptMCMC results

1199 write.table(res,file="Li_MS_570Ma_TimeOptMCMC_results.csv",sep="," ,row.names=FALSE)
1200
1201

```

1202 **References**

1203

1204 61. F. Sun, W. Hu, J. Cao, X. Wang, Z. Zhang, J. Ramezani, S. Shen, Sustained and
1205 intensified lacustrine methane cycling during Early Permian climate warming. *Nat*
1206 *Commun.* 13, 4856 (2022).

1207

1208 62. C.R. Scotese, An Atlas of Phanerozoic Paleogeographic Maps: The Seas Come In
1209 and the Seas Go Out. *Annual Review of Earth and Planetary Sciences.* 49, 679-728
1210 (2021).

1211

1212 63. B.J.W. Mills, C.R. Scotese, N.G. Walding, G.A. Shields, T.M. Lenton, Elevated
1213 CO₂ degassing rates prevented the return of Snowball Earth during the Phanerozoic.
1214 *Nat Commun.* 8, 1110 (2017).

1215

1216 64. J. Fang., H. Wu., Q. Fang., M. Shi., S. Zhang., T. Yang., H. Li., L. Cao.,
1217 Cyclostratigraphy of the global stratotype section and point (GSSP) of the basal
1218 Guzhangian Stage of the Cambrian Period. *Palaeogeography, Palaeoclimatology,*
1219 *Palaeoecology,* 540 (2019).

1220